MASTER

Study of a FDFD-EFIE hybrid method based on mathematical field decomposition

Zweers, M.

Award date:
2006

TU/e technische universiteit eindhoven

Faculty of Electrical Engineering
Division Telecommunication Technology and Electromagnetics
Chair of Electromagnetics

Study of a FDFD-EFIE hybrid method based on mathematical field decomposition

by Mark Zweers

EM-4-06

June, 2006

Report of Master's project performed at
TU/e, Electromagnetics Section and
Onera (Toulouse, France)

Supervisor:
Ir. B.L. Michielsen (Onera)
Dr.ir. M.C. van Beurden (TU/e)
Dr. A. Chabory (TU/e)

Abstract

The finite-difference method provides a fast, accurate and efficient computation of boundary value problems due to its structured, staggered grid. Despite the necessity for numerical radiation conditions, the method is very popular for the computation of electromagnetic scattering. However, this popularity does not reflect the applicability to a broad class of problems: when the scattering object is of arbitrary shape, the structured grid is no longer conformal to the scatterer and consequently the method loses its accuracy. In these cases, an integral-equation method, based on Galerkin discretisation, is often used to solve the scattering problem. Its inconveniences, however, are the computationally more expensive matrix inversion and higher memory usage. A hybrid method has been studied to benefit from the advantages of both methods: conformity of the grid to the arbitrarily shaped scatterer from the integral-equation method, and accuracy and efficiency from the finite-difference method. The hybridisation is based on a mathematical decomposition of the scattered field, established by a smooth, partitioned truncation function. The expectation is that this partitioning results in a more efficient matrix-vector product, and hence a faster convergence, than with currently available hybrid methods. De field decomposition and the basic functionality of the hybrid method has been validated numerically for a dipole field.

Contents

List of Figures

Preface

After long nights of elaborating mathematics, hunting down bugs and writing the report, this is the result of my graduation internship at the Department of Electromagnetism and Radar of ONERA Toulouse (France), for my Masters Degree of Electrical Engineering at the faculty for Electrical Engineering of the Eindhoven University of Technology (The Netherlands).

The long nights have been preceded by a very interesting research experience under the supervision of Bas Michielsen, from who I have learned not only numerous theoretical and practical aspects of (computational) electromagnetics, but also the jargon of this science in the beautiful French language. I will remember our inspiring discussions, nice chats and your wonderful, musical birthday party at the pitoresque chateau. This all would not have been possible without the always enthousiastic support of my professor and supervisor Anton Tijhuis. Not only with respect to my graduation project itself, but also with respect to the inspiring courses of electromagnetics, which comes for credit of the entire chair of Electromagnetics. Bas, Anton, thank you very much for having me given the opportunity to realise one of my best periods in life this far. I would also like to thank Martijn van Beurden for his corrections, and suggestions for improvements, of this report.

I would also like to thank my neighbours at the campus of SupAéro for helping me out in the first weeks of my French life, and my roommates Andreas and Camille for having such a nice living community together. It goes without saying that mentioning you here implies a friendship I cherish.

The last sentences are normally designated to acknowledge ones close friends and family. Normally. But since my studying period has also been marked by a very dark period, I would like these sentences to be much more than just a cliché. Without the everlasting and unconditional support of my friend Martin, but above all that of my family, Anke, Gerrit and Karin, I would not have been where I am now. Closing the chapter of my final studies symbolises for me the end of that bad chapter. Chapters in my book of live, so positively decorated by your presence.

Mark ZWEERS, Toulouse

Chapter 1

Introduction

1.1 General

Ever since the physicist Enrico Fermi numerically simulated the microscopical, statistical mechanisms of heat conduction in solids, with the aid of "the Maniac", a computer built after the ideas and under supervision of the mathematician John Von Neumann in 1952 (see [8]), many numerical methods have been studied and implemented to simulate a variaty of physical phenomena. A very popular numerical method for electromagnetism is the finite-difference method, as introduced in the classical publication by Yee in 1966 (see [23]). In this publication, he presents an application of the leap-frog scheme[1] to Maxwell's curl equations. Although many different finite-difference schemes have been developed for the computation of fluid dynamics and thermo dynamics (see [11]), the leap-frog scheme is still the most popular method in computational electromagnetics. This is due to its accuracy, relatively simple implementation and the fact that most electromagnetic scattering problems are linear. In this linear case, the staggered grid is in close correspondence with the mathematical interpretation of Maxwell's curl equations. However, because of reasons explained further on, this method is often used in combination with other numerical methods like integral-equation methods. These so-called hybrid methods try to benefit from the advantages of the combined methods, while avoiding their inconveniences as much as possible.

The method studied in this report is a frequency-domain hybrid method between an integral-equation method with Galerkin discretisation (sometimes referred to as the Method of Moments (MoM)), and the standard finite-difference method, based on central differences on a structured, staggered grid. The hybrid method is dedicated to the computation of electromagnetic scattering from thin, perfectly electrically conducting (PEC) wires or surfaces of arbitrary shape. The motivation of this study is not only to regularise the discontinuous scattered field for the use of finite differences on the structured grid, but also to obtain a more efficient discretisation of the integral equation. The study covers a theoretical description of the method and a numerical validation with the decomposition of a dipole field. At the time of writing this report, the hybrid method

[1] i.e., a time domain finite-difference (FDTD) method with central differences on a staggered, structured grid

has not been completely implemented.

1.2 The Finite-Difference Method

The frequency domain finite-difference method (FDFD) is based on the discretisation of Maxwell's equations by central differences, achieved by sampling the electromagnetic field at a staggered, structured rectangular grid for the domain of computation (see [23,21,11,7]). Advantages of this method are:

- Accuracy: central differences at a structured grid results locally in second order accuracy.
- Efficiency: a low-cost matrix-vector product, due to its sparse matrix or due to the possible implementation as an operator.
- Low memory usage: there is no need to store the coordinates of these samples of the fields in the domain since they are distributed uniformly in the domain of computation.
- Consistency: when a solution of the numerical matrix equation exists, simultaneous infinite refinement of the mesh in each spatial dimension will result locally in the exact solution.
- Dissipation: the leap-frog scheme is free from numerical dissipation.

Disadvantages of the finite-difference method are:

- The field between two gridpoints must be smooth.
- Localisation: due to the staggered grid and the non-conformity of this grid to the scattering object, the source distributions on the boundary of a scatterer and hence the discontinuity of the scattered field, cannot be well defined on this grid.
- Radiation: the radiation conditions (at infinity) must be simulated numerically at the boundary of the (finite) domain of computation because this domain is not naturally bounded.
- Dispersion: the finite-difference method is spatially numerically dispersive, i.e., the numerical phase velocity depends on the number of samples per wavelength.

The non-conformity to the scattering object, the localisation of the source distribution and the required smoothness of the electromagnetic field between grid points are the most important disadvantages of the finite-difference method with respect to the arbitrary shape of a scattering object. A FDTD-MoM-hybrid method, based on a domain decomposition, has already been developed to embed an arbitrarily shaped scatterer in a structured grid, in order to couple electromagnetically various scatterers (see [5,6]). However, this method does *not* gain efficiency for a single scatterer compared to a pure integral-equation method with Galerkin discretisation.

1.3 The Integral-Equation Method

The integral-equation method with Galerkin discretisation computes numerically the surface-current density on the scatterer, by a discretisation of both this surface distribution and the integral equation on finite (boundary) elements on the scatterer. The advantages of this method are:

- Localisation: since the grid is conformal to the scatterer by definition, source distributions on the scatterer can be well defined (localised) on the grid.
- Radiation: The method does not require numerical radiation conditions, because the domain is bounded naturally by the scatterer.

Disadvantages of the integral-equation method with Galerkin discretisation are:

- Efficiency: the method will result in a full matrix since it requires an interaction of the surface distribution and the electromagnetic field on the entire surface. This full matrix results in an expensive matrix-vector product.
- High memory usage: the full matrix and the absence of a structured grid results in a high memory usage.

Several numerical methods have been developed to deal with the problem of the expensive matrix-vector product due to the Galerkin discretisation. A very popular method is the Fast-Multipole Method (FMM) and several of its derivations, like Multi-level FMM. However, these methods will *not* be considered in this study.

1.4 The Hybrid Method

The integral-equation method and the finite-difference method will be hybridised by a decomposition of the scattered field to a regular and a singular field, where the former is to be solved by the finite-difference method and the latter is to be solved by the integral-equation method. Since the integral-equation method computes the surface-current density on the scatterer, by which the discontinuity of the scattered field is parametrised, the singular field is to contain this discontinuity *exactly*. It will be localised in a small region around the entire scatterer, achieved by a spatial truncation of the integral representation of the scattered field. The regular field is defined as the difference between the scattered field and the singular field. Since the finite-difference method requires the regular field to be smooth (i.e., continuous and continuous differentiable), the truncation for the singular field must be achieved by a smooth truncation function.

The integral equation has to be solved numerically for the surface-current density on the entire surface, implying that no benefit is taken yet from the advantages of the finite-difference method. To do benefit from its advantages, the surface-current density will also be truncated by a smooth truncation function. This truncation will be partitioned, such that the surface-current

density, and hence the integral equation, is localised on a part of the surface. This localisation is a grouping of the boundary elements on which the surface-current density is discretised. Due to this grouping, the interaction between the current elements is localised on a small region on the scatterer. However, due to the interaction of the surface current on the entire scatterer, the grouped boundary elements must interact on the entire scatterer as well. This is achieved by also partitioning the truncation function for the singular field, such that the integral representation of the scattered field is localised in a small region around a part of the scatterer only. The grouped current elements will now interact globally by the regular field, to be computed by the finite-difference method.

Truncation of the surface-current density, and hence local interaction of the current elements, will result in a sparser matrix than that with global interaction of the current elements, as with a pure integral-equation method based on Galerkin discretisation. The global interaction between the partitioned singular field by the regular field will introduce two coupling-operator matrices, which create (secondary) volume sources for the two hybridised methods. As implied by the smoothness of the truncation, these volume sources for the regular field will be smooth, as required by the finite difference method.

The two coupling-operator matrices and the operator matrices of the two hybridised methods will result in a larger system of discrete equations than with one of the two pure methods seperately. However, due to the partitioning of the truncation, the coupling-operator matrices will be sparse. Together with the sparse operator matrix for the finite-difference method and that of the localised integral equation, the entire operator will be sparse. Therefore the method is expected to result in an efficient and accurate computation of the scattered electromagnetic field on a structured grid from an arbitralily shaped scatterer.

1.5 Outline of the report

The basic theory of electromagnetics is presented in Chapter 2. This starts by stating Maxwell's equations and the constitutive relations, supplemented by the jump conditions across a transition layer between two media. Next, the scattering problem is formulated as a boundary-value problem, where the scatterer is represented by some interior domain in free space and the scattered field is to be calculated on the corresponding exterior domain in free space. Next, the boundary-value problem is defined in the entire free space by modelling the scatterer as an infinitesimally thin surface or wire. Then the decomposition of the scattered field is presented, followed by the definition of the resulting operator. The truncation functions are defined in the last paragraph.

Chapter 3 describes the numerics, starting by the definition of the discrete truncation functions. Then the structured, staggered grid in the free space and the finite-element grid on the scatterer are presented. This comes with the discretisation of the operator, consisting of the finite-difference equations on the structured grid, the Galerkin discretisation of the partitioned integral equation on the finite-element grid and the implied coupling operators. The numerical radiation

conditions, required by the finite-difference method, are presented in the end of this chapter.

Chapter 4 presents the results of the various numerical experiments. First, the numerical radiation condition in the boundary layer is verified with the computation a modal field from its boundary values. This quasi-one-dimensional problem allows for a straightforward investigation of the various parameters of the boundary layer. After having deduced the optimal settings for these parameters, the hybrid method will be partially validated by the numerical computation of a dipole field from its decomposition.

Chapter 5 presents the conclusions from this study, followed by recommendations for future research.

Chapter 2

Problem definition

"(...) and God saith: 'Let light be'; and light is." (Genesis 1:3).

2.1 Genesis

The above citation, taken from Genesis 1:3 of Young's Literal Translation (of the Bible, see [1]), indicates the beginning of the (re)creation of the Earth by the division of light and dark. Light can be seen physically as an electromagnetic phenomenon, governed by the study of electromagnetism. And Maxwell saith:

$$\nabla \times \mathbf{H} - \partial_t \mathbf{D} = \mathbf{J}, \tag{2.1a}$$
$$\nabla \times \mathbf{E} + \partial_t \mathbf{B} = -\mathbf{K}. \tag{2.1b}$$

These equations form a system of coupled, linear partial differential equations for vector-valued functions, where $\mathbf{B}$ and $\mathbf{H}$ are the magnetic volume flux density and magnetic volume field strength, respectively, and $\mathbf{D}$ and $\mathbf{E}$ are the electric volume flux density and electric volume field strength, respectively. These are supposed to be smooth (i.e. continuous and continuously differentiable) on the domain, let's say $\Omega^+ \times R_+$, where Maxwell's equations hold:

$$\{\mathbf{E}, \mathbf{H}\} \in C^2(\Omega^+ \times R_+), \tag{2.2a}$$
$$\{\mathbf{B}, \mathbf{D}\} \in C^2(\Omega^+ \times R_+), \tag{2.2b}$$

and are related by the constitutive relations:

$$\mathbf{D} = \bar{\varepsilon}\mathbf{E}, \tag{2.3a}$$
$$\mathbf{B} = \bar{\mu}\mathbf{H}, \tag{2.3b}$$

where $\bar{\varepsilon}$ and $\bar{\mu}$ are the permittivity and the permeability of the medium, respectively. The bar denotes that these quantities are tensor valued, allowing for an anisotropic medium.

In the frequency domain, Maxwell's equations are stated as:

$$\nabla \times \mathbf{H} - j\omega\bar{\varepsilon}\mathbf{E} = \mathbf{J}, \tag{2.4a}$$
$$\nabla \times \mathbf{E} + j\omega\bar{\mu}\mathbf{H} = -\mathbf{K}, \tag{2.4b}$$

where $\mathbf{J}$ and $\mathbf{K}$ are the electric volume-current density and the magnetic volume-current density, respectively. The magnetic volume-current density is defined here for duality only, which will be used in the next chapter. These volume-current densities can be decomposed into a primary and secondary component:

$$\{\mathbf{J},\mathbf{K}\} := \{\mathbf{J},\mathbf{K}\}^{pri} + \{\mathbf{J},\mathbf{K}\}^{sec}, \tag{2.5}$$

where the primary component represents the impressed volume-current density and the secondary component represents the induced volume-current density. With the relations

$$\mathbf{J}^{sec} = \bar{\sigma}^{E}\mathbf{E}, \tag{2.6a}$$
$$\mathbf{K}^{sec} = \bar{\sigma}^{H}\mathbf{H}, \tag{2.6b}$$

where $\bar{\sigma}^{E}$ and $\bar{\sigma}^{H}$ are the electric and magnetic conductivity tensors, respectively, Maxwell's equations can be written as:

$$\nabla \times \mathbf{H} - j\omega\bar{\varepsilon}\mathbf{E} - \bar{\sigma}^{E}\mathbf{E} = \mathbf{J}^{pri}, \tag{2.7a}$$
$$\nabla \times \mathbf{E} + j\omega\bar{\mu}\mathbf{H} + \bar{\sigma}^{H}\mathbf{H} = -\mathbf{K}^{pri}. \tag{2.7b}$$

Now the complex permittivity and complex permeability can be defined by:

$$\bar{\varepsilon}_c := \bar{\varepsilon} + \frac{\bar{\sigma}^{E}}{j\omega} = \bar{\varepsilon} - j\frac{\bar{\sigma}^{E}}{\omega}, \tag{2.8a}$$
$$\bar{\mu}_c := \bar{\mu} + \frac{\bar{\sigma}^{H}}{j\omega} = \bar{\mu} - j\frac{\bar{\sigma}^{H}}{\omega}. \tag{2.8b}$$

With these complex constitutive parameters, Maxwell's equations can be written as:

$$\nabla \times \mathbf{H} - j\omega\bar{\varepsilon}_c\mathbf{E} = \mathbf{J}^{pri}, \tag{2.9a}$$
$$\nabla \times \mathbf{E} + j\omega\bar{\mu}_c\mathbf{H} = -\mathbf{K}^{pri}. \tag{2.9b}$$

For non-static fields, auxiliary equations can be derived [19]:

$$\nabla \cdot \mathbf{B} = 0, \tag{2.10a}$$
$$\nabla \cdot \mathbf{D} = \rho, \tag{2.10b}$$
$$\nabla \cdot (\mathbf{J} + j\omega\mathbf{D}) = 0. \tag{2.10c}$$

The set of differential equations is supplemented by the jump conditions across a smooth transition layer[1] s of two media (denoted by $[]_s$) on the tangential field components and the normal field components, respectively:

$$[\mathbf{n}\times\mathbf{H}]_s = \mathbf{J}_s, \tag{2.11a}$$
$$[\mathbf{n}\times\mathbf{E}]_s = \mathbf{0}; \tag{2.11b}$$

$$[\mathbf{n}\cdot\mathbf{B}]_s = 0, \tag{2.12a}$$
$$[\mathbf{n}\cdot\mathbf{D}]_s = \rho_s, \tag{2.12b}$$

where for a general vector field $\mathbf{A}$:

$$[\mathbf{n}\times\mathbf{A}]_s := \mathbf{n}\times(\mathbf{A}_2-\mathbf{A}_1), \tag{2.13a}$$
$$[\mathbf{n}\cdot\mathbf{A}]_s := \mathbf{n}\cdot(\mathbf{A}_2-\mathbf{A}_1), \tag{2.13b}$$

with $\mathbf{n}$ is the normal vector, pointing from region 1 to region 2. These jump conditions mean that the tangential component of the magnetic field and the normal component of the electric field are in general discontinuous across s. These discontinuities are represented by the induced surface-current density $\mathbf{J}_s$ and the induced surface-charge density ρ_s, respectively. On the contrary, the tangential component of the electric field and the normal component of the magnetic field are continuous across such a layer.

The discontinuity of the electric volume-current density $\mathbf{J}$ satisfies the following relation (see [15]):

$$-\nabla_s\cdot\mathbf{J}_s - j\omega\rho_s = [\mathbf{n}\cdot\mathbf{J}]_s, \tag{2.14}$$

where $[\mathbf{n}\cdot\mathbf{J}]_s$ denotes the jump of the electric volume-current density across the transition layer s.

In a source-free configuration, $\mathbf{J}^{pri} = \mathbf{K}^{pri} = \mathbf{0}$. Then, the conservation law of surface charge (surface continuity) is obtained[2], which is similar to the conservation of volume charge. The equations are given by, respectively:

$$\nabla\cdot\mathbf{J} + j\omega\rho = 0, \tag{2.15a}$$
$$\nabla_s\cdot\mathbf{J}_s + j\omega\rho_s = [\mathbf{n}\cdot\mathbf{J}^{sec}]_s. \tag{2.15b}$$

From now on, only source-free configurations will be considered.

Since only electromagnetic field *radiation* in a homogeneous, source-free medium will be treated, the fields described in this report must also satisfy the homogeneous Helmholtz equation (i.e. the reduced wave equation in [12]):

$$(\nabla^2 + k^2)\mathbf{E} = 0, \tag{2.16a}$$
$$(\nabla^2 + k^2)\mathbf{H} = 0. \tag{2.16b}$$

[1] A definition of a smooth surface can be found in [12]

[2] A very elegant derivation of surface continuity from volume continuity is presented in [22].

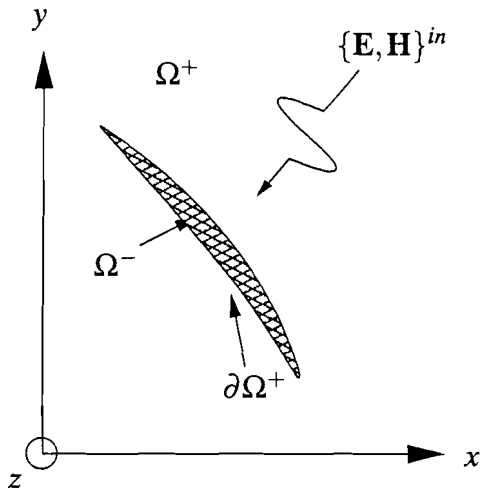

Figure 2.1: An electromagnetic field incident on a thin scatterer, represented by the domain $(\Omega^- \cup \partial\Omega^+) \subset \mathbb{R}^3$

2.2 The boundary-value problem

The scattering problem will be described mathematically as a boundary-value problem on an unbounded (exterior) domain Ω^+ with its boundary $\partial\Omega^+$. The scatterer will be represented by the domain Ω^- with its boundary $\partial\Omega^-$, such that $\partial\Omega^+ = \partial\Omega^-$ (see Figure 2.1):

$$\begin{aligned} \nabla \times \mathbf{H} - j\omega\tilde{\varepsilon}\mathbf{E} &= \mathbf{0} \quad \text{on } \Omega^+, \\ \nabla \times \mathbf{E} + j\omega\tilde{\mu}\mathbf{H} &= \mathbf{0} \quad \text{on } \Omega^+, \\ \mathbf{n} \times \mathbf{E} &= \mathbf{0} \quad \text{on } \partial\Omega \end{aligned} \tag{2.17}$$

The electromagnetic field can be decomposed to an incident electromagnetic field and a scattered electromagnetic field. The incident electromagnetic field is defined as the electromagnetic field in absence of the scatterer. Therefore, it is continuous and continuously differentiable on $\mathbb{R}^3 = \Omega^+ \cup \Omega^- \cup \partial\Omega$. The scattered field is defined as:

$$\mathbf{E}^{sc} := \mathbf{E} - \mathbf{E}^{in}, \tag{2.18a}$$

$$\mathbf{H}^{sc} := \mathbf{H} - \mathbf{H}^{in}. \tag{2.18b}$$

Since Maxwell's equations are linear and required to hold for the incident field on $\mathbb{R}^3$, the scattering problem can now be defined as the boundary-value problem for the scattered field on Ω^+:

$$\begin{aligned} \nabla \times \mathbf{H}^{sc} - j\omega\tilde{\varepsilon}\mathbf{E}^{sc} &= \mathbf{0} \quad \text{on } \Omega^+, \\ \nabla \times \mathbf{E}^{sc} + j\omega\tilde{\mu}\mathbf{H}^{sc} &= \mathbf{0} \quad \text{on } \Omega^+, \\ \mathbf{E}^{sc}_{tg} &= -\mathbf{E}^{in}_{tg} \quad \text{on } \partial\Omega^+. \end{aligned} \tag{2.19}$$

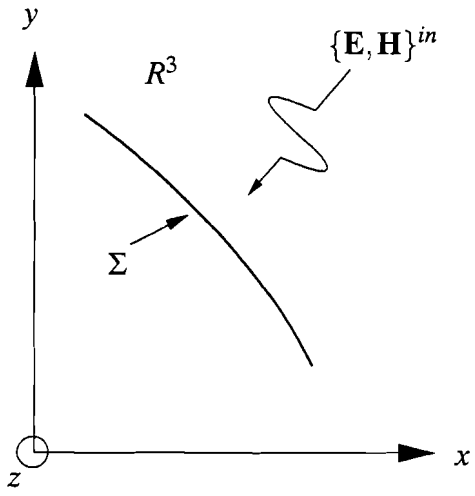

Figure 2.2: An electromagnetic field, incident on a infinitesimally thin scatter, represented by the infinitesimally thin, double-sided surface Σ

For a unique solution of Helmholtz' equations for the scattered field, extra boundary conditions, known as the radiation conditions, are required (see [22, 12]):

$$\lim_{r\to\infty} r\left[Z_0\mathbf{r}_0 \times \mathbf{H}^{sc} + \mathbf{E}^{sc}\right] := \mathbf{0}, \tag{2.20a}$$

$$\lim_{r\to\infty} r\left[Z_0\mathbf{H}^{sc} - \mathbf{r}_0 \times \mathbf{E}^{sc}\right] := \mathbf{0}, \tag{2.20b}$$

$$\{\mathbf{E},\mathbf{H}\} = O\left(\frac{1}{r}\right), \tag{2.20c}$$

where Z_0 is the wave impedance in vacuum and $\mathbf{r}_0 := \frac{\mathbf{r}}{r}$. These conditions imply that, asymptotically, the scattered electromagnetic field is locally a TEM-wave, vanishing at infinity. With these conditions, the term radiation can be defined as the solution of the wave equation propagating from the scatterer towards infinity. From now on, the radiation conditions will be left implicit.

As motivated in the introduction, the aim is to use finite differences with a structured grid on $\mathbb{R}^3$ for numerical computation of the scattered field. However, the boundary-value problem is stated in the domain Ω^+ and on its boundary $\partial\Omega$ only. For this, the thin scatterer will be modelled by an infinitesimally thin, double sided, orientable surface Σ on $\mathbb{R}^3$. This is depicted in Figure 2.2.

The scattered field is now discontinuous across this surface, representable by its two tangential components on this surface:

$$[\mathbf{n}\times\mathbf{H}^{sc}]_s^{\Sigma} = \mathbf{J}_s^{\Sigma}, \tag{2.21a}$$

$$[\mathbf{n}\times\mathbf{E}^{sc}]_s^{\Sigma} = \mathbf{0}. \tag{2.21b}$$

The scattering problem can now be formulated on $\mathbb{R}^3$ as:

$$\begin{aligned} \nabla \times \mathbf{H}^{sc} - j\omega\tilde{\varepsilon}\mathbf{E}^{sc} - \mathbf{J}^{\Sigma} &= \mathbf{0} \quad \text{on } \mathbb{R}^3, \\ \nabla \times \mathbf{E}^{sc} + j\omega\tilde{\mu}\mathbf{H}^{sc} &= \mathbf{0} \quad \text{on } \mathbb{R}^3, \\ \mathbf{E}^{sc}_{tg} &= -\mathbf{E}^{in}_{tg} \quad \text{on } \Sigma, \end{aligned} \tag{2.22}$$

where $\mathbf{J}^{\Sigma}$ is the volume distribution on $\mathbb{R}^3$, corresponding to the surface distribution $\mathbf{J}^{\Sigma}_s$ on Σ.

2.3 Field decomposition

Now that the scattered field is defined as a discontinuous field on $\mathbb{R}^3$, the problem arises that a structured grid on $\mathbb{R}^3$ is generally not conformal to the (arbitrarily shaped) scatterer. The discontinuity of the scattered field is therefore possibly located between grid points, which is in contradiction with the restriction that the field must be smooth between these points. To overcome this problem, the scattered field is decomposed into a smooth (regular) and a discontinuous (singular) component:

$$\{\mathbf{E},\mathbf{H}\}^{sc} := \{\mathbf{E},\mathbf{H}\}^{sng} + \{\mathbf{E},\mathbf{H}\}^{reg}. \tag{2.23}$$

To define these components, the scattered field is first written in terms of the source distributions via the potentials $\mathbf{A}$ and ϕ, according to [22], [15]:

$$\mathbf{H}^{sc} = \nabla \times \mathbf{A} \quad \text{on } \mathbb{R}^3 \setminus \Sigma, \tag{2.24a}$$

$$\mathbf{E}^{sc} = -j\omega\tilde{\mu}\mathbf{A} - \frac{\nabla\phi}{\tilde{\varepsilon}} \quad \text{on } \mathbb{R}^3 \setminus \Sigma. \tag{2.24b}$$

These potentials are given by:

$$\mathbf{A}(\mathbf{r}) := \int_{\Sigma} G_{\mathbf{r}} \mathbf{J}^{\Sigma}_s dA, \tag{2.25a}$$

$$\phi(\mathbf{r}) := \int_{\Sigma} G_{\mathbf{r}} \rho^{\Sigma}_s dA, \tag{2.25b}$$

where $G_{\mathbf{r}}$ is the frequency-domain Green function in free space:

$$G_{\mathbf{r}} : \mathbb{R}^3 \to C \quad \text{by} \quad G_{\mathbf{r}} : \mathbf{r}' \mapsto G_{\mathbf{r}}(\mathbf{r}'), \tag{2.26}$$

with

$$G_{\mathbf{r}}(\mathbf{r}') = \frac{e^{-jk||\mathbf{r}-\mathbf{r}'||}}{4\pi||\mathbf{r}-\mathbf{r}'||}. \tag{2.27}$$

The expressions given in (2.24a) and (2.24b) must satisfy Maxwell's equations. This implies a relation between the scalar and the vector potential, which is given by:

$$\nabla \cdot \mathbf{A} = -j\omega\phi, \tag{2.28}$$

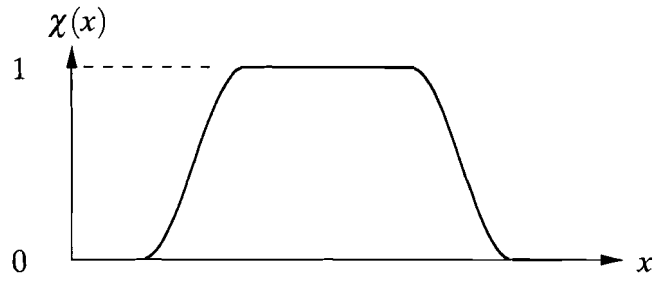

Figure 2.3: An example of a one-dimensional truncation function $\chi(x)$. This function equals unity inside, and zero outside a certain region (in this case an interval on x).

which is known as the Lorenz gauge. It follows directly from the continuity of surface charge (2.15b).

The scattered field, in a homogeneous medium, can now be written as:

$$\mathbf{H}^{sc} = \nabla \times \mathbf{A} \qquad \text{on } \mathbb{R}^3 \setminus \Sigma, \tag{2.29a}$$

$$\mathbf{E}^{sc} = \frac{1}{j\omega\bar{\varepsilon}} \nabla \times \nabla \times \mathbf{A} = \frac{1}{j\omega\bar{\varepsilon}} \{\nabla\nabla\cdot + k^2\} \mathbf{A} \qquad \text{on } \mathbb{R}^3 \setminus \Sigma, \tag{2.29b}$$

where the second equality in (2.29b) is obtained by using the identity (A.6).

Next, these integral representations of the scattered field are spatially truncated by a function χ. A truncation function is a function which equals unity in a certain region, and equals zero outside this region. Truncating the scattered field therefore causes this field to be nonzero in a limited region around Σ only. An example of a truncation function is given by Figure 2.3. The truncation function must be chosen such, that the resulting regular field is smooth on $\mathbb{R}^3$. This implies that the truncation must be smooth on $\mathbb{R}^3$.

The following definitions of the singular field have been studied:

$$\mathbf{H}_1^{sng} := \chi \nabla \times \mathbf{A}, \tag{2.30a}$$

$$\mathbf{E}_1^{sng} := \frac{1}{j\omega\bar{\varepsilon}} \chi \nabla \times \nabla \times \mathbf{A} = \frac{1}{j\omega\bar{\varepsilon}} \chi \{\nabla\nabla\cdot + k^2\} \mathbf{A} =$$

$$= \frac{1}{j\omega\bar{\varepsilon}} \nabla \times \mathbf{H}_1^{sng} - \frac{1}{j\omega\bar{\varepsilon}} \nabla\chi \times \nabla \times \mathbf{A}; \tag{2.30b}$$

$$\mathbf{H}_2^{sng} := \nabla \times \chi \mathbf{A}, \tag{2.30c}$$

$$\mathbf{E}_2^{sng} := \frac{1}{j\omega\bar{\varepsilon}} \nabla \times \nabla \times \chi \mathbf{A} = \frac{1}{j\omega\bar{\varepsilon}} \nabla \times \mathbf{H_2}^{sng}; \tag{2.30d}$$

$$\mathbf{H}_3^{sng} := \mathbf{H}_1^{sng} = \chi \nabla \times \mathbf{A}, \tag{2.30e}$$

$$\mathbf{E}_3^{sng} := \frac{1}{j\omega\bar{\varepsilon}} \nabla \times \chi \nabla \times \mathbf{A} = \frac{1}{j\omega\bar{\varepsilon}} \nabla \times \mathbf{H}_1^{sng}; \tag{2.30f}$$

$$\mathbf{E}_4^{sng} := \mathbf{E}_1^{sng} = \frac{1}{j\omega\bar{\varepsilon}} \chi \nabla \times \nabla \times \mathbf{A} = \frac{1}{j\omega\bar{\varepsilon}} \chi \{\nabla\nabla\cdot + k^2\} \mathbf{A}, \tag{2.30g}$$

$$\mathbf{H}_4^{sng} := \frac{1}{k^2} \nabla \times \chi \{\nabla\nabla\cdot + k^2\} \mathbf{A} = -\frac{1}{j\omega\bar{\mu}} \nabla \times \mathbf{E}_4^{sng}. \tag{2.30h}$$

The choice for these four definitions of the singular field are based on the observation that, from Equations (2.29a) and (2.29b), either the potential, its curl or its double curl can be truncated. With the definitions given by the expressions (2.30c)-(2.30h), one of the two Maxwell equations is satisfied. This will result in a zero-block of the operator matrix (as will be shown further), which might be advantageous.

It is important to emphasize that the singular field is to represent the discontinuity of the scattered field *exactly*, and that $\{\mathbf{E},\mathbf{H}\}^{sng}$ and $\{\mathbf{E},\mathbf{H}\}^{reg}$ do *not* satisfy Maxwell's equations separately. This is due to the fact that the separate fields are non-physical, since the truncation of the scattered field contradicts with the analyticity on $\mathbb{R}^3$ of solutions of Maxwell's equations.

2.4 The operators

Since the total scattered field satisfies Maxwell's equations on $\mathbb{R}^3$, the sum of the singular and regular parts must also satisfy these equations:

$$\begin{pmatrix} \nabla\times & -j\omega\bar{\varepsilon} \\ j\omega\bar{\mu} & \nabla\times \end{pmatrix} \begin{pmatrix} \mathbf{H}^{reg} \\ \mathbf{E}^{reg} \end{pmatrix} + \begin{pmatrix} \nabla\times & -j\omega\bar{\varepsilon} \\ j\omega\bar{\mu} & \nabla\times \end{pmatrix} \begin{pmatrix} \mathbf{H}^{sng} \\ \mathbf{E}^{sng} \end{pmatrix} + \begin{pmatrix} \mathbf{0} \\ -\mathbf{J}^{\Sigma} \end{pmatrix} = \begin{pmatrix} \mathbf{0} \\ \mathbf{0} \end{pmatrix}. \tag{2.31}$$

Elaborating this equation for the four definitions of the singular field, with the aid of the identities in Appendix A, yields:

$$\begin{pmatrix} \nabla\times & -j\omega\bar{\varepsilon} \\ j\omega\bar{\mu} & \nabla\times \end{pmatrix} \begin{pmatrix} \mathbf{H}_1^{sng} \\ \mathbf{E}_1^{sng} \end{pmatrix} = \begin{pmatrix} \nabla\chi\times[\nabla\times\mathbf{A}] \\ \nabla\chi\times\frac{1}{j\omega\bar{\varepsilon}}\{\nabla\nabla\cdot+k^2\}\mathbf{A} \end{pmatrix}, \tag{2.32a}$$

$$\begin{pmatrix} \nabla\times & -j\omega\bar{\varepsilon} \\ j\omega\bar{\mu} & \nabla\times \end{pmatrix} \begin{pmatrix} \mathbf{H}_2^{sng} \\ \mathbf{E}_2^{sng} \end{pmatrix} = \begin{pmatrix} \mathbf{0} \\ \frac{1}{j\omega\bar{\varepsilon}}\nabla\times\nabla\times\nabla\times\chi\mathbf{A}+j\omega\bar{\mu}\nabla\times\chi\mathbf{A} \end{pmatrix}, \tag{2.32b}$$

$$\begin{pmatrix} \nabla\times & -j\omega\bar{\varepsilon} \\ j\omega\bar{\mu} & \nabla\times \end{pmatrix} \begin{pmatrix} \mathbf{H}_3^{sng} \\ \mathbf{E}_3^{sng} \end{pmatrix} = \begin{pmatrix} \mathbf{0} \\ \frac{1}{j\omega\bar{\varepsilon}}\left[\nabla\chi\times\{\nabla\nabla\cdot+k^2\}\mathbf{A}+\nabla\times(\nabla\chi\times\nabla\times\mathbf{A})\right] \end{pmatrix}, \tag{2.32c}$$

$$\begin{pmatrix} \nabla\times & -j\omega\bar{\varepsilon} \\ j\omega\bar{\mu} & \nabla\times \end{pmatrix} \begin{pmatrix} \mathbf{H}_4^{sng} \\ \mathbf{E}_4^{sng} \end{pmatrix} = \begin{pmatrix} \chi\nabla\times\mathbf{A}+\frac{1}{k^2}\nabla\chi\times\{\nabla\nabla\cdot+k^2\}\mathbf{A}-\chi\{\nabla\nabla\cdot+k^2\}\mathbf{A} \\ \mathbf{0} \end{pmatrix}, \tag{2.32d}$$

where the curly brackets $\{\}$ are used to distinguish between an operator acting on the following term and a multiplication of two terms.

With Equation (2.25a), Equations (2.32a)-(2.32d) can be expressed in terms of the surface current $\mathbf{J}_s^{\Sigma}$. The operator-matrix equation (2.31) can now be written as:

$$[\mathbf{M}]\begin{pmatrix} \mathbf{H}^{reg} \\ \mathbf{E}^{reg} \end{pmatrix} + [\mathbf{C}_1]\mathbf{J}_s^{\Sigma} := \begin{pmatrix} \mathbf{0} \\ \mathbf{0} \end{pmatrix}, \tag{2.33}$$

where

$$[\mathbf{M}] := \begin{pmatrix} \nabla\times & -j\omega\bar{\varepsilon} \\ j\omega\bar{\mu} & \nabla\times \end{pmatrix}. \tag{2.34}$$

The operator matrix $\mathbf{C}_1$ is an expansion operator, coupling the parametrisation of the singular field to Maxwell's equations for the regular field. It can therefore be seen as a source for the field described by the differential equations.

Singular field decomposition (2.32b) introduces third-order derivatives of the truncation function χ; it will therefore not be considered any further.

Elaborating the surface condition in boundary-value problem (2.22) for the decomposed scat-

tered field on Σ gives:

$$\begin{aligned}\mathbf{E}_{tg}^{reg}+\mathbf{E}_{1,tg}^{sng}&=\mathbf{E}_{tg}^{reg}+\mathbf{E}_{4,tg}^{sng}=\mathbf{E}_{tg}^{reg}+\left[\frac{1}{j\omega\bar{\varepsilon}}\chi\nabla\times\nabla\times\mathbf{A}\right]_{tg}\\&=\mathbf{E}_{tg}^{reg}+\left[\frac{1}{j\omega\bar{\varepsilon}}\chi\{\nabla\nabla\cdot+k^2\}\mathbf{A}\right]_{tg}\\&=-\mathbf{E}_{tg}^{in},\end{aligned}\tag{2.35}$$

and:

$$\begin{aligned}\mathbf{E}_{tg}^{reg}+\mathbf{E}_{3,tg}^{sng}&=\mathbf{E}_{tg}^{reg}+\left[\frac{1}{j\omega\bar{\varepsilon}}\nabla\times\chi\nabla\times\mathbf{A}\right]_{tg}\\&=\mathbf{E}_{tg}^{reg}+\left[\frac{1}{j\omega\bar{\varepsilon}}\chi\{\nabla\nabla\cdot+k^2\}\mathbf{A}\right]_{tg}+\left[\frac{1}{j\omega\bar{\varepsilon}}\nabla\chi\times\nabla\times\mathbf{A}\right]_{tg}\\&=-\mathbf{E}_{tg}^{in},\end{aligned}\tag{2.36}$$

respectively, which can again be written in terms of the surface current $\mathbf{J}_s^{\Sigma}$. This will result in the operator-matrix equation:

$$[\mathbf{C}_2']\mathbf{E}^{reg}+[\mathbf{BIE}]\mathbf{J}_s^{\Sigma}=-\mathbf{E}_{tg}^{in},\tag{2.37}$$

where $[\mathbf{C}_2']$ is the trace operator on Σ, and $[\mathbf{BIE}]$ is the boundary integral operator on Σ. The presence of the regular field on Σ must be interpreted physically by the fact that $\mathbf{H}_{tg}^{reg}$ and $\mathbf{E}_{nm}^{reg}$ are smooth on Σ, but not necessarily zero.

With the aid of Equations (2.33) and (2.37), boundary-value problem (2.22) can be written in operator-matrix form as:

$$\begin{pmatrix}[\mathbf{M}] & [\mathbf{C}_1]\\ [\mathbf{C}_2] & [\mathbf{BIE}]\end{pmatrix}\begin{pmatrix}\mathbf{H}^{reg}\\ \mathbf{E}^{reg}\\ \mathbf{J}_s^{\Sigma}\end{pmatrix}=\begin{pmatrix}\mathbf{0}\\ \mathbf{0}\\ -\mathbf{E}_{tg}^{in}\end{pmatrix},\tag{2.38}$$

where

$$[\mathbf{C}_2]=\begin{pmatrix}\mathbf{0} & \mathbf{0}\\ \mathbf{0} & [\mathbf{C}_2']\end{pmatrix},\tag{2.39}$$

the Maxwell operator matrix.

2.5 The truncation functions

As stated in the previous section, definitions (2.30c) and (2.30d) for the singular field will not be used because of the implied third-order derivatives of χ. This is due to the choice for χ to be a

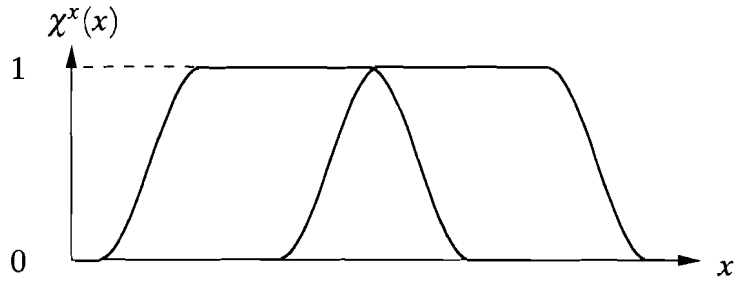

Figure 2.4: An example of the partitioning of a one-dimensional truncation function $\chi(x)$. This partitioning is a decomposition of the truncation function to partial truncation functions.

smooth function:

$$\chi \in C^2(\mathbb{R}^3), \tag{2.40a}$$

in correspondance with Equations (2.2a) and (2.2b).

As motivated in the introduction, the method will only be useful with a partitioned truncation function for the singular field and for the surface-current density. The partitioning of a truncation function is a decomposition of that function in partial truncation functions. This is depicted in Figure 2.4. This partitioning implies the definition of a set X of partial truncation functions χ_k, and the definition of a set Ψ of partial truncation functions ψ_k. This results in a partitioning of the singular field:

$$\mathbf{H}^{sng} = \sum_k \mathbf{H}_k^{sng}, \tag{2.41a}$$

$$\mathbf{E}^{sng} = \sum_k \mathbf{E}_k^{sng}, \tag{2.41b}$$

and in a partitioning of the surface-current density:

$$\mathbf{J}_{s,k}^{\Sigma} = \psi_k \mathbf{J}_s^{\Sigma}. \tag{2.42}$$

Consequently, the integral representations for the partitioned singular field can be written as:

$$\mathbf{H}_{1,k}^{sng} = \chi_k \nabla \times \int_{\Sigma_k} \psi_k G_{\mathbf{r}} \mathbf{J}_s^{\Sigma} dA, \tag{2.43a}$$

$$\mathbf{E}_{1,k}^{sng} = \frac{\chi_k}{j\omega\bar{\varepsilon}} \{\nabla\nabla\cdot + k^2\} \int_{\Sigma_k} \psi_k G_{\mathbf{r}} \mathbf{J}_s^{\Sigma} dA, \tag{2.43b}$$

from which the truncation of the surface-current density can be interpreted as a localisation of Green's kernel of the integral representation. Numerically, this is be a grouping of the boundary elements on which the surface-current density is sampled (see the next chapter). This localisation

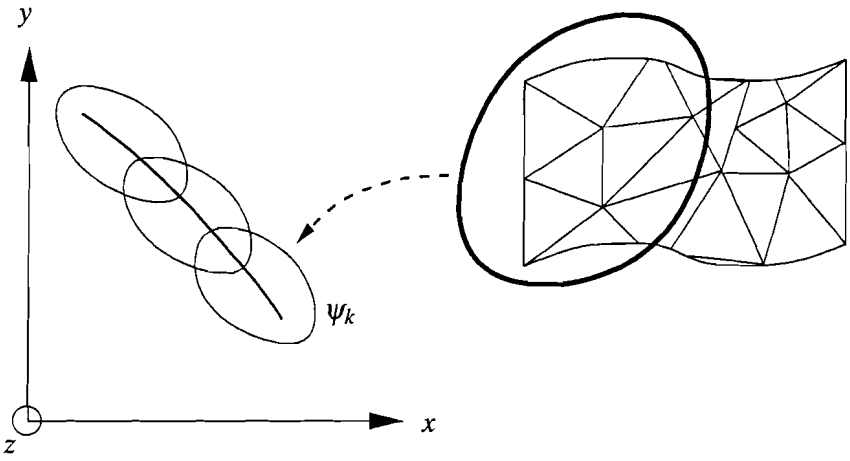

Figure 2.5: An impression of the support of partial truncation functions. The trace of these truncation functions on the scatterer results in the partitioned truncation of the surface-current density. This is a localisation of Green's kernel of the integral representation, which numerically is a grouping of the current elements.

is depicted in Figure 2.5. Since the regular field is continuous in $\mathbb{R}^3$ by definition, the discontinuity of the scattered field is now represented entirely by the jump of the tangential components of the singular magnetic field:

$$[\mathbf{n}\times\mathbf{H}_k^{sc}]_s = [\mathbf{n}\times\mathbf{H}_k^{sng}]_s = [\mathbf{n}\times\chi_k\nabla\times\int_{\Sigma_k}\psi_k G_{\mathbf{r}}\mathbf{J}_s^{\Sigma}dA]_s. \tag{2.44}$$

As shown in [10], this results in:

$$[\mathbf{n}\times\mathbf{H}_k^{sc}]_s = \chi_k\psi_k\mathbf{J}_s^{\Sigma}. \tag{2.45}$$

Two choices can now be made, based upon the aim to represent the parametrisation of the discontinuity in the singular field *exactly*:

i) the total surface current is represented exactly by a summation of partial surface currents, as defined by Equation (2.42);

ii) the trace of χ on Σ equals ψ, such that the surface current is represented exactly by Equation (2.50)

Elaborating the first choice, results in:

$$\mathbf{J}_s^{\Sigma} = \sum_k \psi_k\mathbf{J}_s^{\Sigma}, \tag{2.46}$$

which implies that Ψ is a partition of unity on Σ, with local support (see [2]):

$$\begin{array}{lll} \text{i)} & \forall_{\psi_k \in \Psi} \vee \forall_{x \in \mathbb{R}^3} & : 0 \leq \psi_k(x) \leq 1, \\ \text{ii)} & \forall_k \forall_{x \notin U_k} & : \psi_k(x) = 0, \\ \text{iii)} & \forall_{x \in \Sigma} & : \sum_k \psi_k = 1, \\ \text{iv)} & \forall_{\psi_k \in \Psi} & : \operatorname{supp} \psi_k(x) \subseteq U_k, \end{array} \tag{2.47}$$

where $U_k \in U$ is a spatial region, covering a part of Σ. Together with Equation (2.50), this restricts χ_k to equal unity on the *entire* support of ψ_k:

$$\chi_k = 1 \quad on \quad \operatorname{supp}(\psi_k), \tag{2.48}$$

since otherwise the partition of unity for Ψ will be violated. This result implyies that the trace of χ on Σ is *not* a partition of unity, and hence $\nabla\chi \neq \mathbf{0}$.

The second choice implies that the trace of χ at Σ equals ψ:

$$\operatorname{tr}(\chi_k)_\Sigma = \psi_k. \tag{2.49}$$

Then, from the continuity of the tangential components of $\mathbf{H}^{reg}$ and Equation (2.23):

$$[\mathbf{n} \times \mathbf{H}_k^{sc}]_s = [\mathbf{n} \times \mathbf{H}_k^{sng}]_s = (\psi_k)^2 \mathbf{J}_s^\Sigma. \tag{2.50}$$

From Equation (2.41b), the total surface current will then be:

$$\mathbf{J}^\Sigma = \sum_k (\psi_k)^2 \mathbf{J}^\Sigma. \tag{2.51}$$

Define $\varphi_k := (\psi_k)^2 \in \Phi$, then Equation (2.51) restricts Φ to be a partition of unity on Σ, satisfying the same conditions as for (2.46). This choice again implies that the trace of χ on Σ is *not* a partition of unity, and hence again $\nabla\chi \neq \mathbf{0}$.

Chapter 3

Numerics

3.1 The truncation functions

The truncation is elaborated for the case where $\mathrm{tr}(\chi)_\Sigma = \psi$, such that $\mathrm{tr}(\varphi)_\Sigma := \psi^2$. It is most easily implemented with respect to the structured, rectangular grid in $\mathbb{R}^3$. This rectangularity of the grid allows the truncation function to be a product of functions in each Cartesian coordinate of the grid:

$$\tilde{\varphi}^{\alpha}_{\mathbf{r}_{i,j,k}} := \tilde{\varphi}^{\alpha}_{x}\tilde{\varphi}^{\alpha}_{y}\tilde{\varphi}^{\alpha}_{z} = \sum_{k} \varphi^{\alpha}_{x,k}\varphi^{\alpha}_{y,k}\varphi^{\alpha}_{z,k}, \tag{3.1}$$

where the function $\varphi^{\alpha}_{x,p}[i]$ is the p-th local truncation function, defined on the p-th covering of Σ, in the x-direction. It containing α cells of the structured grid. For this function $\varphi_{x,p}$, three regions can be identified:

I $\varphi_{x,p}$ equals unity in a finite region around its center,

II $\varphi_{x,p}$ smoothly decays to a value of $\frac{1}{2}$ where two partial truncation functions intersect,,

III $\varphi_{x,p}$ equals zero at the cell edges.

Further, due to the structured grid, $\varphi_{x,p}$ must be symmetrical with respect to the cell edges and cell corners of its support (i.e., the interval where the function does not equal zero). It should be emphasized that this support is several times the mesh size of the structured grid. The above observations are depicted in Figure 3.1a for the one-dimensional truncation function. A resulting two-dimensional truncation function is depicted in Figure 3.1b. The following function for $\varphi_{x,p}[i]$

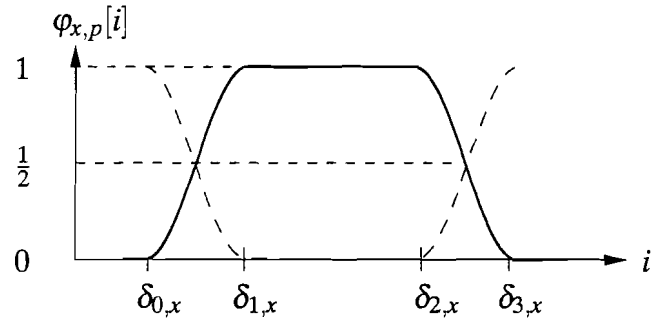

(a) A one-dimensional partial truncation function

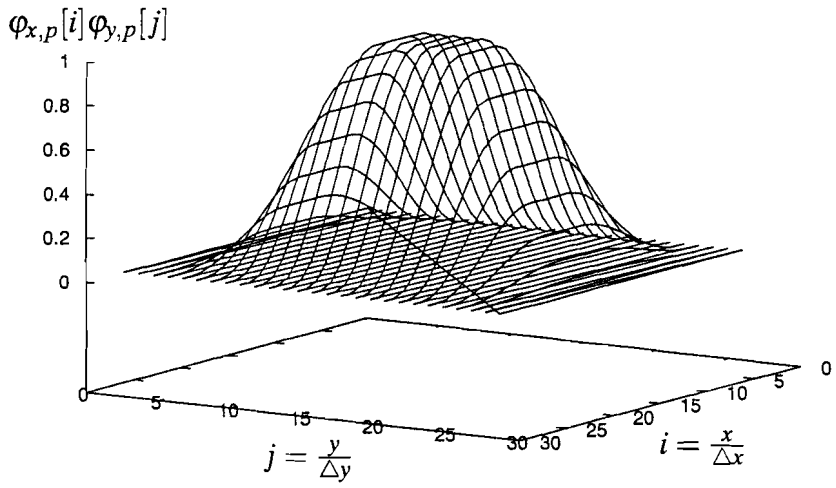

(b) A two-dimensional partial truncation function

Figure 3.1: The partial truncation function, where the δ's define the region where the truncation function equals unity, the transition region of the truncationfunction and the region where the truncation function equals zero.

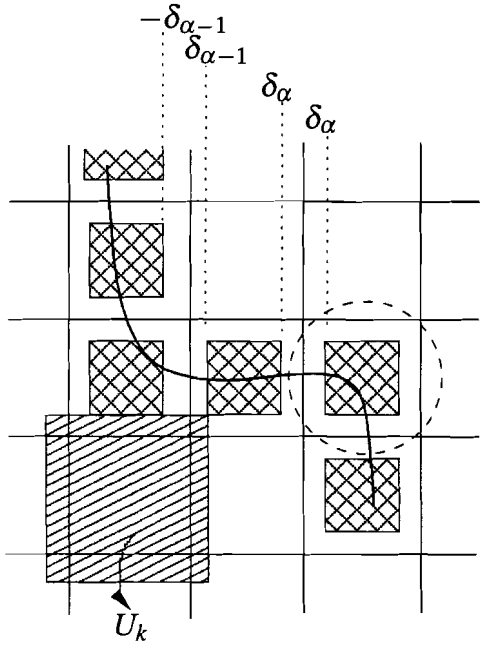

Figure 3.2: An impression of the truncation of the scattered field in the case of a thin wire as scattering object.

has been chosen:

$$\varphi_{x,p}[i] := \begin{cases} \frac{1}{2}\left[1+\cos\left(\frac{\pi(i_p-\delta_{x,1})}{2\delta_{x,1}}\right)\right] & ;\delta_{x,0} < i_p < \delta_{x,1}, \\ \frac{1}{2}\left[1-\cos\left(\frac{\pi(i_p-\delta_{x,3})}{2\delta_{x,3}}\right)\right] & ;\delta_{x,2} < i < \delta_{x,3}, \\ 1 & ;\delta_{x,1} < i < \delta_{x,2} \\ 0 & ;i < \delta_{x,0} \wedge i > \delta_{x,3}, \end{cases} \tag{3.2}$$

where the δ_x's are depicted in Figure 3.1a, and where i_p parametrises the x-coordinate on the support of the p-th truncation function.

The functions $\varphi_y^\alpha[j]$ and $\varphi_z^\alpha[k]$ are defined similarly. The gradient of this truncation function still is a smooth function, its Laplacian or higher-order derivatives (which appear in the definitions of the singular field) are discontinuous. These discontinuities create spurious (current) sources on the structured grid, and should therefore be avoided. Therefore, only Expressions (2.30a) and (2.30b) will be used as definitions for the singular field.

Figure 3.2 finally gives an impression of how the truncation of the scattered field should be partitioned in the case of a thin wire as scattering object.

The chosen definition of the truncation function allows for two parameters to adjust:

- the size of the region where the truncation equals unity,
- the size of the transition region.

However, when the transition region is taken too small with respect to the mesh size, the numerical approximation of the truncation functions will introduce spurious singular terms and hence spurious surface currents on Σ.

3.2 The difference equations

The sampling of the fields in $\mathbb{R}^3$ will be defined on a structured, staggered rectangular grid. To define this grid on $\mathbb{R}^3$, the cartesian positioning vector is discretised:

$$\mathbf{r} := x\mathbf{u}_x + y\mathbf{u}_y + z\mathbf{u}_z \approx \mathbf{r}_{ijk}, \tag{3.3}$$

with

$$\mathbf{r}_{ijk} := i\triangle_x\mathbf{u}_x + j\triangle_y\mathbf{u}_y + k\triangle_z\mathbf{u}_z =: x_i\mathbf{u}_x + y_j\mathbf{u}_y + z_k\mathbf{u}_z \quad i,j,k \in \mathbb{Z}. \tag{3.4}$$

The various field components are sampled on:

$$\begin{array}{lll} E_x: & x = x_{i+\frac{1}{2}}, & y = y_j, \quad z = z_k, \\ E_y: & x = x_i, & y = y_{j+\frac{1}{2}}, \quad z = z_k, \\ E_z: & x = x_i, & y = y_j, \quad z = z_{k+\frac{1}{2}}, \\ H_x: & x = x_i, & y = y_{j+\frac{1}{2}}, \quad z = z_{k+\frac{1}{2}}, \\ H_y: & x = x_{i+\frac{1}{2}}, & y = y_j, \quad z = z_{k+\frac{1}{2}}, \\ H_z: & x = x_{i+\frac{1}{2}}, & y = y_{j+\frac{1}{2}}, \quad z = z_k. \end{array} \tag{3.5}$$

For reasons of implementation, a single-parameter notation has been used to formulate the difference equations. For this, the Cartesian components $\{x,y,z\}$ are indexed with $w \in \{0,1,2\}$, respectively. Index calculations are implemented by adding an integer modulo 3 to the index, such that the components x,y,z will maintain there mutual ordening. This is represented by the symbol $+_3$.

Next, the sampling of the field components on this grid is written in terms of the index w. For this, two matrices are defined with the discretised position vector for the v-th cartesian component in

the v-th column:

$$[\mathbf{e}](i,j,k) := \begin{pmatrix} x_{i+\frac{1}{2}} & x_i & x_i \\ y_j & y_{j+\frac{1}{2}} & y_j \\ z_k & z_k & z_{k+\frac{1}{2}} \end{pmatrix}, \tag{3.6a}$$

$$[\mathbf{h}](i,j,k) := \begin{pmatrix} x_i & x_{i+\frac{1}{2}} & x_{i+\frac{1}{2}} \\ y_{j+\frac{1}{2}} & y_j & y_{j+\frac{1}{2}} \\ z_{k+\frac{1}{2}} & z_{k+\frac{1}{2}} & z_k \end{pmatrix}. \tag{3.6b}$$

$[\mathbf{e}]$ and $[\mathbf{h}]$ are related by:

$$[\mathbf{h}] = [\mathbf{e}] + [\mathbf{b}], \tag{3.7}$$

where

$$[\mathbf{b}] := \frac{1}{2} \begin{pmatrix} -\triangle_x & \triangle_x & \triangle_x \\ \triangle_y & -\triangle_y & \triangle_y \\ \triangle_z & \triangle_z & -\triangle_z \end{pmatrix}. \tag{3.8}$$

The discretised position vectors $\mathbf{e}_w$ and $\mathbf{b}_w$ are defined as the w-th column of the matrices $[\mathbf{e}]$ and $[\mathbf{b}]$, respectively.

The difference equations for the fields, sampled at the structured grid, are now given by:

$$\begin{aligned} &\frac{1}{\triangle_{w+3\,2}}\Big(E_{w+3\,2}[\mathbf{e}_{w+3\,2} - \mathbf{d}_{w+3\,1}] - E_{w+3\,2}[\mathbf{e}_{w+3\,2}]\Big) \\ &- \frac{1}{\triangle_{w+3\,1}}\Big(E_{w+3\,1}[\mathbf{e}_{w+3\,1} + \mathbf{d}_{w+3\,2}] - E_{w+3\,1}[\mathbf{e}_{w+3\,1}]\Big) \\ &+ j\omega\bar{\mu}_w H_w[\mathbf{e}_w + \mathbf{b}_w] = 0, \end{aligned} \tag{3.9a}$$

$$\begin{aligned} &\frac{1}{\triangle_{w+3\,2}}\Big(H_{w+3\,2}[\mathbf{e}_{w+3\,2} + \mathbf{b}_{w+3\,2}] - H_{w+3\,2}[\mathbf{e}_{w+3\,2} + \mathbf{b}_{w+3\,2} - \mathbf{d}_{w+3\,1}]\Big) \\ &- \frac{1}{\triangle_{w+3\,2}}\Big(H_{w+3\,1}[\mathbf{e}_{w+3\,1} + \mathbf{b}_{w+3\,1}] - H_{w+3\,1}[\mathbf{e}_{w+3\,1} + \mathbf{b}_{w+3\,1} - \mathbf{d}_{w+3\,2}]\Big) \\ &- j\omega\bar{\varepsilon}_w E_w[\mathbf{e}_w] = 0, \end{aligned} \tag{3.9b}$$

where $\mathbf{d}_w$ is defined as w-th collumn-vector of $[\mathbf{d}]$:

$$[\mathbf{d}] := \begin{pmatrix} -\triangle_0 & 0 & 0 \\ 0 & -\triangle_1 & 0 \\ 0 & 0 & -\triangle_2 \end{pmatrix}. \tag{3.10}$$

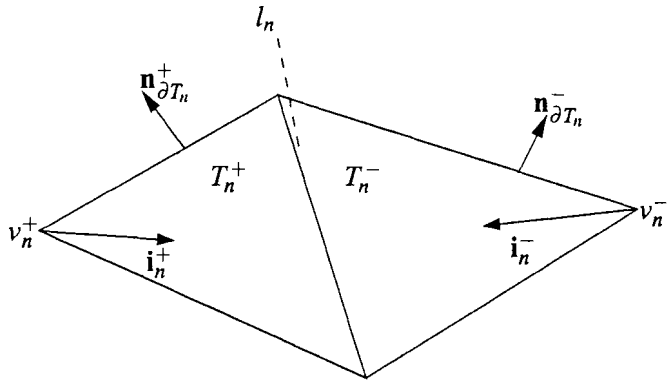

Figure 3.3: The two elements of the n-th RWG basis function corresponding to the n-th non-boundary edge

3.3 The integral equation

The surface-current density $\mathbf{J}_s^\Sigma$ is sampled by an expansion in triangular basis functions on Σ, according to [14]:

$$\mathbf{J}_s^\Sigma \approx \sum_{n=0}^{N} I_n \mathbf{f}_n, \tag{3.11}$$

where $\mathbf{f}_n$ is the n-th basis function, defined with respect to the n-th non-boundary edge in the finite-element space. Since such an edge is always the common one for two elements, the basis functions exist of two elements. The elements are usually denoted by $+, -$, where the sign can be chosen according to the direction of the surface current. One such basis function is depicted in Figure 3.3, and is defined as:

$$\mathbf{f}_n := \begin{cases} \dfrac{l_n}{2A_n^\pm}\mathbf{i}_n^\pm(\mathbf{r}) & \mathbf{r} \in T_n^\pm, \\ 0 & \text{elsewhere}, \end{cases} \tag{3.12}$$

where, $A_n^\pm$ is the area of triangle $T_n^\pm$, l_n is de length of the n-th non-boundary edge and $\mathbf{i}_n^\pm(\mathbf{r})$ is the position vector for a point $\mathbf{r} \in T_n^\pm$, with respect to the vertex $v_n^\pm$. The factor $\frac{l_n}{2A_n^\pm}$ normalises the basis functions, such that the normal component of the surface-current density is continuous across the common edge of their triangles and hence no (spurious) line charges are induced. Despite the fact that several authors have published about these basis functions[1], in electromagnetics they are usually referred to as the RWG basis functions.

[1]The more general case of a volume discretisation is described in detail in a.o. [13]

The surface divergence is given by:

$$\nabla_s \cdot \mathbf{f}_n := \begin{cases} \pm \dfrac{l_n}{A_n^{\pm}} & \mathbf{r} \in T_n^{\pm}, \\ 0 & \text{elsewhere.} \end{cases} \tag{3.13}$$

Together with the truncation function for the current, ψ, the discretised vector potential $\mathbf{A}$ becomes:

$$\begin{aligned} \mathbf{A}(\mathbf{r}) &\approx \int_{T_n} G_{\mathbf{r}}(\mathbf{r}')\psi \sum_{n=0}^{N} I_n \mathbf{f}_n(\mathbf{r}')dA = \sum_{n=0}^{N} \int_{T_n} G_{\mathbf{r}}(\mathbf{r}')\psi \mathbf{f}_n(\mathbf{r}')I_n dA \\ &= \sum_{n=0}^{N} \Big(\frac{l_n}{2A_n^+} \int_{T_n^+} G_{\mathbf{r}}(\mathbf{r}')\psi \mathbf{i}_n^+(\mathbf{r}')dA + \frac{l_n}{2A_n^-} \int_{T_n^-} G_{\mathbf{r}}(\mathbf{r}')\psi \mathbf{i}_n^-(\mathbf{r}')dA \Big) I_n. \end{aligned} \tag{3.14}$$

Note that

$$\frac{1}{2A_n^-} \int_{T_n} G_{\mathbf{r}}\psi \mathbf{i}_n(\mathbf{r}')dA = \frac{1}{2}\Big(G_{\mathbf{r}}\psi \mathbf{i}_n(\mathbf{r}')\Big)^{\mathrm{AVG},n}, \tag{3.15}$$

where AVG,n denotes the average value in the n-th element. For far-field calculations (relative to the dimensions of triangle), the value at the barycenter (i.e. the center of mass) of each triangle, as proposed in [14], is a good approximation of this average value. However, $\mathbf{H}^{sng}$ and $\mathbf{E}^{sng}$ are required on gridpoints in the near-field zone of each triangle. A seven-point Gaussian quadrature integration rule has been implemented, with the aim to obtain a more accurate near-field approximation:

$$\frac{1}{2A_n^{\pm}} \int_{T_n} G_{\mathbf{r}}\psi \mathbf{i}_n^{\pm}(\mathbf{r}')dA \approx \sum_{p=0}^{P} w_n^{\pm}(\mathbf{r}_p) G_{\mathbf{r}}(\mathbf{r}_p)\psi \mathbf{i}_n^{\pm}(\mathbf{r}_p), \tag{3.16}$$

where where $w_n^{\pm}(\mathbf{r}_p)$ is the weighting factor for the p-th abscis. The approximation of the vector potential can now be written as:

$$\mathbf{A}(\mathbf{r}) \approx \sum_{n=0}^{N} \sum_{p=0}^{P} l_n \Big(w_{np}^+ G_{\mathbf{r}}(\mathbf{r}_p)\psi \mathbf{i}_n^+(\mathbf{r}_p) + w_{np}^- G_{\mathbf{r}}(\mathbf{r}_p)\psi \mathbf{i}_n^-(\mathbf{r}_p) \Big) I_n. \tag{3.17}$$

To discretise the integral equation, (i.e., the discretisation of the operator $[\mathbf{BIE}]$ in Equation (2.38)), Equations (2.35) and (2.36) will be tested by the same functions as the basis function (3.12). Testing these equations gives:

$$\begin{aligned} < \mathbf{f}_m, -\mathbf{E}_{tg}^{in} > &= < \mathbf{f}_m, \mathbf{E}_{tg}^{reg} + \frac{1}{j\omega\bar{\varepsilon}} \chi \{ \nabla\nabla\cdot + k^2 \} \mathbf{A} > \\ &= < \mathbf{f}_m, \mathbf{E}_{tg}^{reg} > + \frac{1}{j\omega\bar{\varepsilon}} < \mathbf{f}_m, \chi \{ \nabla\nabla\cdot + k^2 \} \mathbf{A} >, \end{aligned} \tag{3.18}$$

and

$$< \mathbf{f}_m, -\mathbf{E}_{tg}^{in} > = < \mathbf{f}_m, \mathbf{E}_{tg}^{reg} + \frac{1}{j\omega\bar{\varepsilon}} \left(\chi \left\{\nabla\nabla\cdot + k^2\right\} \mathbf{A} > + \nabla\chi \times \nabla \times \mathbf{A}\right) >$$
$$= < \mathbf{f}_m, \mathbf{E}_{tg}^{reg} > + \frac{1}{j\omega\bar{\varepsilon}} \left(< \mathbf{f}_m, \chi \left\{\nabla\nabla\cdot + k^2\right\} \mathbf{A} > + < \mathbf{f}_m, \nabla\chi \times \nabla \times \mathbf{A} > \right), \quad (3.19)$$

respectively, where linearity is used.

First, the second term in both equations is elaborated. This gives for Equation (3.18):

$$< \mathbf{f}_m, \chi \left\{\nabla\nabla\cdot + k^2\right\} \mathbf{A} > = \int_{T_m} \mathbf{f}_m \cdot \chi \left\{\nabla\nabla\cdot + k^2\right\} \mathbf{A} dA$$
$$= \int_{T_m} \mathbf{f}_m \cdot \chi \nabla\nabla\cdot \mathbf{A} dA + \int_{T_m} \mathbf{f}_m \cdot \chi k^2 \mathbf{A} dA, \quad (3.20)$$

of which the first term can be rewritten as:

$$\int_{T_m} \mathbf{f}_m \cdot \chi \nabla\nabla\cdot \mathbf{A} dA = \int_{T_m} \nabla \cdot \left(\chi \mathbf{f}_m \nabla\cdot \mathbf{A}\right) dA - \int_{T_m} \nabla\cdot \mathbf{A} \nabla \cdot (\chi \mathbf{f}_m) dA =$$
$$= \int_{\partial T_m} \mathbf{n}_\partial \cdot \left(\chi \mathbf{f}_m \nabla\cdot \mathbf{A}\right) dl - \int_{T_m} \nabla\cdot \mathbf{A} \nabla \cdot (\chi \mathbf{f}_m) dA, \quad (3.21)$$

where $T_m = T_m^+ \cup T_m^-$ is the union of the two triangles of the m-th non-boundary edge, and $\mathbf{n}_\partial \mathbf{T_m} = \mathbf{n}_{\partial T_m}^+ \cup \mathbf{n}_{\partial T_m}^-$ (depicted in Figure 3.3) is the constant normal vector on the boundary ∂T_m.

Since by definition of the test functions no line charges or currents exist, the contour integral is equal but opposite of sign for two adjacent triangles and therefore, for non-boundary triangles, the contour integral vanishes. Elaborating the second term of (3.21) results in:

$$< \mathbf{f}_m, \chi \left\{\nabla\nabla\cdot + k^2\right\} \mathbf{A} > = - \int_{T_m} \nabla\cdot \mathbf{A} \chi \nabla \cdot \mathbf{f}_m dA - \int_{T_m} \nabla\cdot \mathbf{A} \mathbf{f}_m \cdot \nabla\chi dA + \int_{T_m} \chi k^2 \mathbf{f}_m \cdot \mathbf{A} dA. \quad (3.22)$$

Equation (3.20) can now be rewritten as:

$$< \mathbf{f}_m, \chi \left\{\nabla\nabla\cdot + k^2\right\} \mathbf{A} > = - < \nabla\cdot \mathbf{f}_m, \chi \nabla\cdot \mathbf{A} > - < \mathbf{f}_m \cdot \nabla\chi, \nabla\cdot \mathbf{A} > + < \mathbf{f}_m, \chi k^2 \mathbf{A} > . \quad (3.23)$$

Following the same steps, this yields for (3.19):

$$< \mathbf{f}_m, \chi \left\{\nabla\nabla\cdot + k^2\right\} \mathbf{A} > + < \mathbf{f}_m, \nabla\chi \times \nabla \times \mathbf{A} >$$
$$= - < \nabla\cdot \mathbf{f}_m, \chi \nabla\cdot \mathbf{A} > + < \mathbf{f}_m, \nabla\chi \times \nabla \times \mathbf{A} > + < \mathbf{f}_m, \chi k^2 \mathbf{A} > . \quad (3.24)$$

The transposition of one of the two nablas from the potential to the test function is advantageous since this requires less operations on the unknown potential, while the divergence of the test

functions is calculated analytically. This also holds for the scalar product of the test function with the gradient of the truncation function. For this reason, definition (2.32a) for the singular field seems to be the best choice, and will therefore be the only one further elaborated.

Next, the test functions must be defined. According to [14], these functions will be identical to the basis functions, which is known as the Galerkin method. Substituting for the discretised vector potential (i.e. Equation (3.17) and the test functions $\mathbf{f}_m$, yields for Equation (3.24):

$$\begin{aligned}\int_{T_m} \chi\nabla\cdot\mathbf{A}\nabla\cdot\mathbf{f}_m dA &\approx \int_{T_m} \chi\nabla\cdot\mathbf{f}_m\nabla\cdot\sum_{n=0}^{N}\sum_{p=0}^{P} l_n\Big(w_{np}^{+}G_{\mathbf{r}}(\mathbf{r}_p)\psi\mathbf{i}_n^{+}(\mathbf{r}_p)+w_{np}^{-}G_{\mathbf{r}}(\mathbf{r}_p)\psi\mathbf{i}_n^{-}(\mathbf{r}_p)\Big)I_n dA\\ &= \sum_{n=0}^{N}\sum_{p=0}^{P} l_m l_n\Big[\frac{1}{A_m^{+}}\int_{T_m^{+}} \chi w_{np}^{+}\nabla\cdot\big(G_{\mathbf{r}}(\mathbf{r}_p)\psi\mathbf{i}_n^{+}(\mathbf{r}_p)\big)dA+\frac{1}{A_m^{-}}\int_{T_m^{-}} \chi w_{np}^{-}\nabla\cdot\big(G_{\mathbf{r}}(\mathbf{r}_p)\psi\mathbf{i}_n^{-}(\mathbf{r}_p)\big)dA\Big],\end{aligned} \tag{3.25a}$$

$$\begin{aligned}\int_{T_m} \{\mathbf{f}_m\cdot\nabla\chi\}\nabla\cdot\mathbf{A}dA &\approx \int_{T_m} \{\mathbf{f}_m\cdot\nabla\chi\}\nabla\cdot\sum_{n=0}^{N}\sum_{p=0}^{P} l_n\Big(w_{np}^{+}G_{\mathbf{r}}(\mathbf{r}_p)\psi\mathbf{i}_n^{+}(\mathbf{r}_p)+w_{np}^{-}G_{\mathbf{r}}(\mathbf{r}_p)\psi\mathbf{i}_n^{-}(\mathbf{r}_p)\Big)I_n dA\\ &= \sum_{n=0}^{N}\sum_{p=0}^{P}\frac{l_m l_n}{2}\Big[\frac{1}{A_m^{+}}\int_{T_m^{+}} \{\mathbf{i}_m^{+}(\mathbf{r}_p)\cdot\nabla\chi\}w_{np}^{+}\nabla\cdot\big(G_{\mathbf{r}}(\mathbf{r}_p)\psi\mathbf{i}_n^{+}(\mathbf{r}_p)\big)dA\\ &\quad+\frac{1}{A_m^{-}}\int_{T_m^{-}} \{\mathbf{i}_m^{-}(\mathbf{r}_p)\cdot\nabla\chi\}w_{np}^{-}\nabla\cdot\big(G_{\mathbf{r}}(\mathbf{r}_p)\psi\mathbf{i}_n^{-}(\mathbf{r}_p)\big)dA\Big],\end{aligned} \tag{3.25b}$$

$$\begin{aligned}\int_{T_m} \chi k^2\mathbf{f}_m\cdot\mathbf{A}dA &\approx \int_{T_m} \chi k^2\mathbf{f}_m\cdot\sum_{n=0}^{N}\sum_{p=0}^{P} l_n\Big(w_{np}^{+}G_{\mathbf{r}}(\mathbf{r}_p)\psi\mathbf{i}_n^{+}(\mathbf{r}_p)+w_{np}^{-}G_{\mathbf{r}}(\mathbf{r}_p)\psi\mathbf{i}_n^{-}(\mathbf{r}_p)\Big)I_n dA\\ &= \sum_{n=0}^{N}\sum_{p=0}^{P} l_m l_n\Big[\frac{k^2}{A_m^{+}}\int_{T_m^{+}} \chi w_{np}^{+}\mathbf{i}_m^{+}(\mathbf{r})\cdot\psi\mathbf{i}_n^{+}(\mathbf{r}_p)G_{\mathbf{r}}(\mathbf{r}_p)dA\\ &\quad-\frac{k^2}{A_m^{-}}\int_{T_m^{-}} \chi w_{np}^{-}\mathbf{i}_m^{-}(\mathbf{r})\cdot\psi\mathbf{i}_n^{-}(\mathbf{r}_p)G_{\mathbf{r}}(\mathbf{r}_p)dA\Big].\end{aligned} \tag{3.25c}$$

The physical interpretation of the scalar product $\mathbf{i}_m^{-}(\mathbf{r}_q)\cdot\mathbf{i}_n^{-}(\mathbf{r}_p)$ follows from the interpretation of the basis functions and the test functions: the normal component of the n-th current element doesn't contribute to tangential components of the potential, and vice versa.

3.4 The coupling equations

The operator matrix $[\mathbf{C}_1]$ expands the integral representations of the scattered field to the structured grid in $\mathbb{R}^3$. The following observations can be made:

$$\frac{1}{j\omega\bar{\varepsilon}}\nabla\chi\times\{\nabla\nabla\cdot+k^2\}\mathbf{A} \quad\rightarrow\quad \text{E-grid}, \tag{3.26a}$$

$$\nabla\chi\times\nabla\times\mathbf{A} \quad\rightarrow\quad \text{H-grid}. \tag{3.26b}$$

The surface-current density $\mathbf{J}_s^{\Sigma}$ will be partitioned, as stated in the previous chapter. This implies that the expansion of the above equations on the structured grid can be done for each partial surface current seperately. This expanded singular field on the structured grid will vanish outside the support of the truncation function ϕ, due to the choice of equal truncation functions ψ for the singular field (see Equation (2.49)). Therefore a limited number of samples of the surface current will contribute to the coupling by $[\mathbf{C}_1]$, thereby sparsening this operator matrix. This sparsening is expected to result in a more efficient matrix-vector product.

Second, $[\mathbf{C}_2]\mathbf{E}^{reg}$ is tested. However, this operator will *not* result in some Galerkin-like matrix, since $\mathbf{E}^{reg}$ is not expanded by basis functions. The trace of the regular field components on Σ is computed by a linear interpolation of the field samples on the structured grid to Σ. This interpolation must be computed for all the P points on which the surface-current density is computed; see Equations (3.14)-(3.17). For each Cartesian component ($w\in\{0,1,2\}$) of the approximated surface current, eight corresponding gridpoints are involved. The interpolated electric regular field and the interpolated electric incident field are tested in a similar way as the singular field:

$$<\mathbf{f}_m,\mathbf{E}_{tg}^{reg}>=\sum_{p=0}^{P}\int_{T_m^+\cup T_m^-}\mathbf{f}_m\cdot\mathbf{E}_{tg}^{reg}(\mathbf{r}_p)dA, \tag{3.27a}$$

$$<\mathbf{f}_m,\mathbf{E}_{tg}^{in}>=\sum_{p=0}^{P}\int_{T_m^+\cup T_m^-}\mathbf{f}_m\cdot\mathbf{E}_{tg}^{in}(\mathbf{r}_p)dA. \tag{3.27b}$$

Approximating the integrals gives, respectively:

$$<\mathbf{f}_m,\mathbf{E}_{tg}^{reg}>=\sum_{p=0}^{P}\left(\frac{l_m}{2A_m^+}w_{m,p}^+\mathbf{E}_{tg}^{reg}(\mathbf{r}_p)\cdot\mathbf{i}_m^+(\mathbf{r}_p)+\frac{l_m}{2A_m^-}w_{m,p}^-\mathbf{E}_{tg}^{reg}(\mathbf{r}_p)\cdot\mathbf{i}_m^-(\mathbf{r}_p)\right), \tag{3.28}$$

$$<\mathbf{f}_m,\mathbf{E}_{tg}^{in}>=\sum_{p=0}^{P}\left(\frac{l_m}{2A_m^+}w_{m,p}^+\mathbf{E}_{tg}^{in}(\mathbf{r}_p)\cdot\mathbf{i}_m^+(\mathbf{r}_p)+\frac{l_m}{2A_m^-}w_{m,p}^-\mathbf{E}_{tg}^{in}(\mathbf{r}_p)\cdot\mathbf{i}_m^-(\mathbf{r}_p)\right). \tag{3.29}$$

3.5 The numerical radiation condition

For obvious reasons, the domain of computation must be finite. This is often achieved by implementing a perfectly electrically conducting bounding box around the domain of computation,

such that the electromagnetic field in this interior domain is not transmitted to the exterior domain. If the aim is to simulate the (infinite) free space within the finite domain of computation, the radiation conditions must be simulated at the boundary. For arbitrary radiation[2] in free space, the radiation conditions are simulated by increasing, in a small region near the boundary of the domain of computation, the order of attenuation to an exponential one. When the region is chosen sufficiently large, the fields will become negligable on the boundary of the domain of computation. In this study, the small region near the boundary will be interpreted as an (anisotropically) absorbing material layer. To prevent reflections from occuring on the interface between the background and the boundary layer, the impedance of the material in the boundary layer must be matched to the impedance of the background.

Research on absorbing-material boundary layers has been started with the classical paper of Bérenger (see [3]), in which he presents a perfectly matched layer (PML). However, because "his" PML implies a modification of Maxwell's equations in the boundary layer, it is neither straightforward to implement in a standard finite difference scheme, nor the fields in this boundary layer can be interpreted physically. The absorbing material used here will therefore be an axially anisotropic lossy medium, as described in [17, 9, 24, 25]. Another presentation will be given here, based on [18]. Aim is to avoid the confusingly many (superfluous) variables as in [25] and to give a physically correct interpretation of this boundary layer.

As stated before, the numerical radiation condition is simulated by an exponential decay of electromagnetic radiation towards the boundary of the domain of computation. This exponential attenuation in the boundary layer is achieved by a pull-back transformation of the analytical (complex) continuation of the electromagnetic field, with conservation of its implied exponential behaviour. The analytical continuation is in fact a stretch of the coordinates from the real axis to the complex plane (as described in [7]), transforming a propagating wave to an evanescent wave.

The analytically continuated field must satisfy Maxwell's equations with stretched coordinates:

$$\widehat{\nabla} \times \widehat{\mathbf{H}}' - j\omega\widehat{\mathbf{D}}' = \mathbf{0}, \tag{3.30a}$$

$$\widehat{\nabla} \times \widehat{\mathbf{E}}' + j\omega\widehat{\mathbf{B}}' = \mathbf{0}, \tag{3.30b}$$

where a homogeneous medium is supposed. Quantities in the boundary layer are denoted by a prime $'$ and the analytic continuation is denoted by a $\widehat{\text{hat}}$. Now the analytically continuated fields must be pulled back to the domain of computation, i.e., transformed to the domain with real-valued coordinates. This is achieved by the pull-back transformation V^{-1}:

$$V^{-1} : \mathbb{C}^3 \to \mathbb{R}^3 \quad \text{by} \quad \widehat{\mathbf{r}}' \mapsto \mathbf{r}' = V^{-1}\widehat{\mathbf{r}}'. \tag{3.31}$$

The stretch of a coordinate is chosen to depend only on the direction of that coordinate. Therefore, the transformation matrix $[V]$ can be written in Cartesian coordinates as a diagonal matrix:

$$[V] := diag\{v_x, v_y, v_z\} \quad \in \mathbb{C}^3. \tag{3.32}$$

[2]According to a.o. [4], evanescent waves require boundary conditions other than the radiation conditions mentioned here.

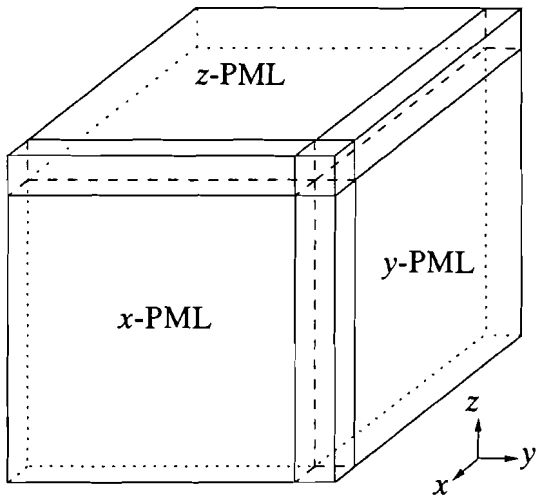

Figure 3.4: An intersection of two PML-faces creates a PML-edge, an intersection of three PML-faces creates a PML-corner. Therefore the stretch of coordinates can be assigned to a PML-face. The names of the PML-faces are chosen according to the direction of the normal vector on each face.

Each corner and each edge in a rectangular domain are formed by an intersection of the orthogonal PML-faces, as depicted in Figure 3.4. Therefore, in Cartesian coordinates, the transformation matrix $[V]$ can be written as a multiplication of the transformation matrices for the PML-faces:

$$[V] := [V]^{(x)}[V]^{(y)}[V]^{(z)}. \tag{3.33}$$

For each PML-face, only the corresponding coordinate is stretched. This yields for, for example, the z-PML:

$$[V]_z^{(x)} = [I], \tag{3.34a}$$
$$[V]_z^{(y)} = [I], \tag{3.34b}$$
$$[V]_z^{(z)} = diag\{1,1,v_z\}, \tag{3.34c}$$

with $[I] := diag\{1,1,1\}$. The continuity conditions for the electromagnetic field incident on an interface between two penetrable media hold:

$$[\![\mathbf{n}\times\mathbf{H}]\!] = \mathbf{n}\times(\mathbf{H}'-\mathbf{H}) = \mathbf{0}, \tag{3.35a}$$
$$[\![\mathbf{n}\times\mathbf{E}]\!] = \mathbf{n}\times(\mathbf{E}'-\mathbf{E}) = \mathbf{0}, \tag{3.35b}$$

and

$$[\![\mathbf{n}\cdot\mathbf{B}]\!] = \mathbf{n}\cdot(\mathbf{B}'-\mathbf{B}) = 0, \tag{3.36a}$$
$$[\![\mathbf{n}\cdot\mathbf{D}]\!] = \mathbf{n}\cdot(\mathbf{D}'-\mathbf{D}) = 0, \tag{3.36b}$$

where the constant normal vector $\mathbf{n}$ points from the background region to the boundary layer.

The stretch of the coordinates implies a transformation of functions with these coordinates. Therefore a transformation V^{*-1} is associated with V^{-1}, transforming Maxwell's equations for the analytically continuated fields to similar curl equations for the pulled-back fields. This associated transformation is defined for general functions f as:

$$V^{*-1} : \mathbb{C}^3 \to \mathbb{R}^3 \quad \text{by} \quad V^{*-1} f \mapsto (Cf) \circ V^{-1}, \tag{3.37}$$

such that

$$\forall_{x \in \mathbb{R}} : f(x) = Cf(V^{-1}\widehat{x}), \tag{3.38}$$

where C is a constant tensor, scaling the naturally induced transformation. By this associated transformation, the curl equations (with non-stretched coordinates), for the pulled-back electromagnetic field in the boundary layer become:

$$(CV\nabla) \times V^{-1}\mathbf{H}' - j\omega V^{-1}\mathbf{D}' = \mathbf{0}, \tag{3.39a}$$

$$(CV\nabla) \times V^{-1}\mathbf{E}' + j\omega V^{-1}\mathbf{B}' = \mathbf{0}. \tag{3.39b}$$

The transformation of the electromagnetic field can now be converted to a transformation of the curl operator, as demonstrated in [7]. However, the aim is to simplify the implementation of the PML. For this, let $C := V^{-2}$. Then, with the aid of the matrix representation in Cartesian coordinates of the pulled-back curl operator:

$$[(V^{-1}\nabla)\times] = \begin{pmatrix} 0 & -\frac{1}{v_z}\partial_z & \frac{1}{v_y}\partial_y \\ \frac{1}{v_z}\partial_z & 0 & -\frac{1}{v_x}\partial_x \\ -\frac{1}{v_y}\partial_y & \frac{1}{v_x}\partial_x & 0 \end{pmatrix}, \tag{3.40}$$

Equations (3.30a) and (3.30b) become:

$$\begin{pmatrix} 0 & -\frac{1}{v_z v_y}\partial_z & \frac{1}{v_y v_z}\partial_y \\ \frac{1}{v_z v_x}\partial_z & 0 & -\frac{1}{v_x v_z}\partial_x \\ -\frac{1}{v_y v_x}\partial_y & \frac{1}{v_x v_y}\partial_x & 0 \end{pmatrix} \mathbf{H}' - j\omega\bar{\varepsilon}[V^{-1}]\mathbf{E}' = \mathbf{0}, \tag{3.41a}$$

$$\begin{pmatrix} 0 & -\frac{1}{v_z v_y}\partial_z & \frac{1}{v_y v_z}\partial_y \\ \frac{1}{v_z v_x}\partial_z & 0 & -\frac{1}{v_x v_z}\partial_x \\ -\frac{1}{v_y v_x}\partial_y & \frac{1}{v_x v_y}\partial_x & 0 \end{pmatrix} \mathbf{E}' + j\omega\bar{\mu}[V^{-1}]\mathbf{H}' = \mathbf{0}. \tag{3.41b}$$

Now the associated transformation for the curl operator and the pull-back transformation of the electromagnetic field can be combined to scale either the curl operator or the material parameters. The latter is elaborated here, for a correspondence with the literature mentioned in the introduction of this paragraph. By this, Maxwell's equations for the electromagnetic field in the PML can be written as:

$$\nabla \times \mathbf{H}' - j\omega[\varepsilon']\mathbf{E}' = \mathbf{0}, \tag{3.42a}$$

$$\nabla \times \mathbf{E}' + j\omega[\mu']\mathbf{H}' = \mathbf{0}, \tag{3.42b}$$

where

$$[\varepsilon'] := [\Lambda][\varepsilon], \tag{3.43a}$$
$$[\mu'] := [\Lambda][\mu], \tag{3.43b}$$

and where

$$[\Lambda] := diag\{\lambda_x, \lambda_y, \lambda_z\} = \begin{pmatrix} \frac{\nu_z \nu_y}{\nu_x} & 0 & 0 \\ 0 & \frac{\nu_z \nu_x}{\nu_y} & 0 \\ 0 & 0 & \frac{\nu_y \nu_x}{\nu_z} \end{pmatrix}. \tag{3.44}$$

Equations (3.42a) and (3.42a) allow for an easy implementation of the PML: the same finite-difference equations can be used in this region, only the material parameters have to be multiplied by a complex number.

In agreement with Equation (3.33), $[\Lambda]$ can be written as:

$$[\Lambda] = [\Lambda]^{(x)}[\Lambda]^{(y)}[\Lambda]^{(z)}. \tag{3.45}$$

From Equation (3.40), the following relation for the λ_w's on the i-PML can be obtained:

$$\lambda_w^i = \frac{1}{\lambda_{w+3\,1}^i} = \frac{1}{\lambda_{w+3\,2}^i} =: \lambda \quad w, i \in \{x, y, z\}, \tag{3.46}$$

so that:

$$[\Lambda]^{(x)} = \begin{pmatrix} \lambda & 0 & 0 \\ 0 & \frac{1}{\lambda} & 0 \\ 0 & 0 & \frac{1}{\lambda} \end{pmatrix}, \quad [\Lambda]^{(y)} = \begin{pmatrix} \frac{1}{\lambda} & 0 & 0 \\ 0 & \lambda & 0 \\ 0 & 0 & \frac{1}{\lambda} \end{pmatrix}, \quad [\Lambda]^{(z)} = \begin{pmatrix} \frac{1}{\lambda} & 0 & 0 \\ 0 & \frac{1}{\lambda} & 0 \\ 0 & 0 & \lambda \end{pmatrix} \tag{3.47}$$

where

$$\lambda = \lambda' - j\lambda'' \in \mathbb{C}; \quad \lambda', \lambda'' \in \mathbb{R}_+, \tag{3.48}$$

when the coordinates in the corresponding direction are stretched.

A comparison of Equation (3.47) with Equations (2.8a) and (2.8b) yields to the interpretation of the PML as a lossy, axially anisotropic medium. This can be seen from the elaboration of the

material parameters of, for example, the z-face of the PML:

$$[\varepsilon]' = \varepsilon_0[\Lambda]^{(z)}[\varepsilon]_r = \varepsilon_0 \begin{pmatrix} \left(\varepsilon_{x,r} + \frac{\sigma_x^E}{j\omega\tilde{\varepsilon}_0}\right)^{-1} & 0 & 0 \\ 0 & \left(\varepsilon_{y,r} + \frac{\sigma_y^E}{j\omega\tilde{\varepsilon}_0}\right)^{-1} & 0 \\ 0 & 0 & \varepsilon_{z,r} + \frac{\sigma_z^E}{j\omega\tilde{\varepsilon}_0} \end{pmatrix}, \tag{3.49a}$$

$$[\mu]' = \mu_0[\Lambda]^{(z)}[\mu]_r = \mu_0 \begin{pmatrix} \left(\mu_{x,r} + \frac{\sigma_x^H}{j\omega\tilde{\mu}_0}\right)^{-1} & 0 & 0 \\ 0 & \left(\mu_{y,r} + \frac{\sigma_y^H}{j\omega\tilde{\mu}_0}\right)^{-1} & 0 \\ 0 & 0 & \mu_{z,r} + \frac{\sigma_z^H}{j\omega\tilde{\mu}_0} \end{pmatrix}, \tag{3.49b}$$

As shown in Appendix B, the interface between the PML and the background is now iso-reflective.

With the background medium being purely real ($[\mu], [\varepsilon] \in \mathbb{R}^{3\times3}$), λ can be interpreted physically as well:

$$\lambda_w' = \varepsilon_{w,r}, \tag{3.50a}$$

$$\lambda_w'' = \frac{\sigma_w^E}{\omega\varepsilon_0} = \frac{\sigma_w^H}{\omega\mu_0}, \tag{3.50b}$$

where σ^E and σ^H are the electric and magnetic conductivity, respectively. The last equality states that

$$\frac{\sigma^E}{\sigma^H} = \frac{\varepsilon_0}{\mu_0}. \tag{3.51}$$

Since there is no need to scale the real part of the constitutive parameters, $\lambda' := 1$. In this case, Equation (3.51) is the matching condition for the PML to the background.

The PML is now easy to implement; the constitutive parameters in this region are multiplied by a complex number only. The difference equations (3.9a) and (3.9b) can therefore be formu-

lated in the entire domain of computation as:

$$\frac{1}{\triangle_{w+_3 2}}\Big(E_{w+_3 2}[\mathbf{e}_{w+_3 2}-\mathbf{d}_{w+_3 1}]-E_{w+_3 2}[\mathbf{e}_{w+_3 2}]\Big)$$
$$-\frac{1}{\triangle_{w+_3 1}}\Big(E_{w+_3 1}[\mathbf{e}_{w+_3 1}-\mathbf{d}_{w+_3 2}]-E_{w+_3 1}[\mathbf{e}_{w+_3 1}]\Big)$$
$$+j\omega\lambda_w\mu_w H_w[\mathbf{e}_w+\mathbf{b}_w]=0, \tag{3.52a}$$

$$\frac{1}{\triangle_{w+_3 2}}\Big(H_{w+_3 2}[\mathbf{e}_{w+_3 2}+\mathbf{b}_{w+_3 2}]-H_{w+_3 2}[\mathbf{e}_{w+_3 2}+\mathbf{b}_{w+_3 2}+\mathbf{d}_{w+_3 1}]\Big)$$
$$-\frac{1}{\triangle_w}\Big(H_{w+_3 1}[\mathbf{e}_{w+_3 1}+\mathbf{b}_{w+_3 1}]-H_{w+_3 1}[\mathbf{e}_{w+_3 1}+\mathbf{b}_{w+_3 1}+\mathbf{d}_{w+_3 2}]\Big)+$$
$$-j\omega\lambda_w\varepsilon_w E_w[\mathbf{e}_w]=0, \tag{3.52b}$$

where λ_w equals unity in the background medium.

According to [3], the thickness of each PML-face should be multiple cells (of the structured grid) in order to achieve sufficient attenuation. To also minimise numerical (spurious) reflections from the interface between the background and the PML, the conductivity of the first PML-layer should not be too large. To satisfy both conditions, the following parametrised profile for λ'' is chosen:

$$\lambda''=\lambda_0''(1+(\frac{|w-w_0|}{\zeta})^m), \tag{3.53}$$

where λ_0'' represents the minimum conductivity (in the first layer of the PML) and $|w-w_0|$ is the position w relative to the position of the interface between the background and the PML w_0. The parameter m allows to adjust the gradient of the conductivity and consequently the attenuation of the electromagnetic power in the PML. The parameter ζ allows to control their maximum values.

Since the exponential attenuation is approximated linearly in each cell of the structure grid, non-physical results can occur when the mesh size is taken too large. This implies an upper limit on the mesh size, e.g. for the z-PML:

$$\lambda_z'' \ll \frac{1}{k_z\triangle_z}, \tag{3.54}$$

where $k_z=\omega\sqrt{\mu_z\varepsilon_z}$ of the background medium, so that

$$\sigma(z)^E \ll \frac{\varepsilon_0}{\triangle_z\sqrt{\mu_z\varepsilon_z}}. \tag{3.55}$$

When the background is a vacuüm, this can be rewritten as:

$$\sigma(z)^E \ll \frac{1}{\triangle_z Z_0}. \tag{3.56}$$

It is here where the parameter ζ is useful: with the formulation in [9], condition (3.54) might be violated when the central-difference scheme is used in this region[3]. Important to notice is that this relation is *independent* of the frequency.

[3] Bérenger used for this purpose an exponential quadrature in the boundary layer to discretise his modified Maxwell equations.

Chapter 4

Validation

As stated in the introduction, the hybrid method has not been completely implemented and hence it has not been verified numerically for "real" scattering problems. In this chapter, a dipole field will therefore be considered as a scattered field, the dipole itself being considered as an induced source. This will be preceded by numerical experiments with the PML, in order to obtain its optimal conductivity profile. With this profile, the numerical reconstruction of the dipole field from its decomposition is presented, where the most important objective is to verify that the singular field vanishes in the region where the truncation function equals unity.

In all the numerical experiments, a BiCG-stab solver (i.e., an iterative method based on squared bi-conjugated gradients, see [16]) has been used to compute iteratively the regular field by the finite-difference equations. The relative error of the n-th iterate vector is defined as the 2-norm of the n-th residue vector, relative to the 2-norm of the right-hand side vector:

$$Err_{rel,n} := \frac{||b - Ax_n||_2}{||b||_2}, \tag{4.1}$$

where $Ax = b$ is the system of equations to be solved iteratively.

It should be emphasized that the boundary value problem is formulated in the frequency domain. For the finite-difference equations, this implies the abscence of the explicit time step, as present in the leap-frog scheme. As a consequence, each iteration does *not* show the propagation of electromagnetic waves, but the numerical propagation of the iterative solution through the domain of computation.

4.1 Modal Field

4.1.1 Experiment

The numerical computation of a modal field in a waveguide allows for a straightforward study of the finite-difference method and the PML, since this numerical field can easily be compared to its

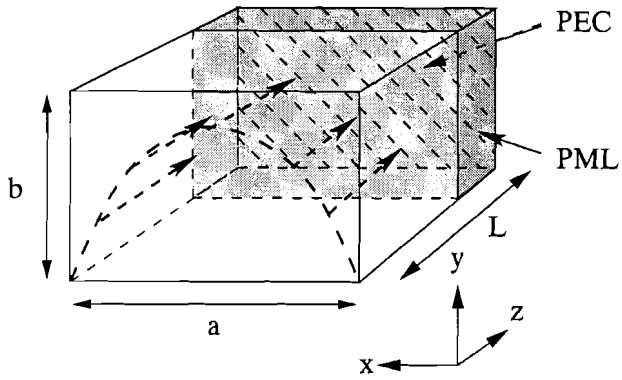

Figure 4.1: The waveguide with the electric field for the TE^z_{10} mode. This configuration requires one PML-face only, backed by a perfectly electrically conducting screen.

analytic counterpart. Furthermore, since a waveguide has only got one open end in the direction of propagation, only one PML-face is needed (the problem is quasi-one-dimensional). The modal field in the domain of computation will be reconstructed numerically from its tangential electric field (boundary values) on one open end of the waveguide, such that the reconstructed modal field will propagate from this open end to the PML. This is shown in Figure 4.1. The configuration is chosen such that the mode will be propagating (see Appendix C.2), and such that no resonances can occur. A TE^z_{10}-mode is chosen:

- $f = 300$ [MHz].
- $b = 0.75$ [m].
- $a = 0.75$ [m].
- $L = 0.50$ [m],

where f is the frequency and a, b, L are the dimensions of the waveguide.

From various numerical experiments, the lowest relative error of the numerical field compared to the analytical field, in a configuration with a homogeneous PML, has been achieved with $\sigma_0^E = 3 \cdot 10^{-2}$ [Sm^{-1}]. When choosing the value of σ_0^E and σ_L^E (where $0, L$ indicates the first and last PM-layer, respectively) such that condition (3.54) is satisfied, variations of the conductivity will result in equal variations of the attenuation. For the case where the conductivity is increased linearly in the PML ($m = 1$), the value of σ_0^E is chosen slightly lower and the value of σ_L^E is chosen slightly higher than those with the homogeneous profile, such that the reflection from the first layer will be less while still providing sufficient attenuation. The following values have been chosen:

$$\sigma_0^E = 1.5 \cdot 10^{-2} \quad [\text{Sm}^{-1}], \tag{4.2a}$$

$$\sigma_L^E = 4.0 \cdot 10^{-2} \quad [\text{Sm}^{-1}], \tag{4.2b}$$

yielding for ζ:

$$\zeta = 0.15 \quad [1]. \tag{4.3}$$

Now the numerical experiments are performed for various values of m[1], with variable σ_0^E. The conductivity profiles are depicted in Figure 4.2a, their corresponding attenuation (accumulative per cell) are depicted in Figure 4.2b. The expectation is that in the homogeneous case, a small σ_0^E will result in considerable reflection from the PEC-boundary, while a large σ_0^E will result in considerable numerical reflection from the first boundary layer. With the non-homogeneous profile, the expectation is that a small value for m will slightly improve the numerical approximation of the interior modal field, while a large value for m will result in non-physical results due to the numerical linear approximation of the attenuation in the PML. For each m, the curves of the relative error of the numerically reconstructed interior modal field are expected to decrease or increase monotoneously towards an optimum value, when σ_0^E is increased or decreased, respectively.

4.1.2 Algorithm

As described in the previous chapter, the domain of computation is bounded by a perfectly electrically conducting bounding box, of which each face is supplied with a PML. The waveguide will be simulated numerically by this bounding box, but now only one face will be supplied with a PML, i.e., acting as the open end of an infinite waveguide. On the opposite face of the boundary of the domain of computation, the tangential electrical modal field will be expandeded. By this, the vector of unknowns, as in Equation (4.1), x can be decomposed as:

$$x := x^i + x^{tg}, \tag{4.4}$$

where x^i represents all the interior (unknown) field components and x^{tg} represents the expanded analytic tangential electric components. Since the face on which x^{tg} is expanded now contains the boundary values for the propagating modal field, it can be seen as the other open end of the waveguide. However, due to implementation, the tangential electric field is set to zero on the boundary of the domain of computation when iteratively solving the operator-matrix equation. Therefore the expanded tangential electric modal field at this boundary will be converted to an equivalent volume magnetic current density b' in the interior of the domain[2]:

$$b' := -[\mathbf{M}]^{tg} x^{tg}, \tag{4.5}$$

such that

$$[\mathbf{M}]^i x^i = b + b', \tag{4.6}$$

where $b := 0$ since no impressed volume sources are present. Distinction is made between the Maxwell-operator matrix acting on the boundary values (^{tg}) and the Maxwell-operator matrix acting on the interior values (^{i}), since their ranks are different. However, the same Maxwell-operator matrix has been used for the numerical computation. Equation (4.6) is now the equation for the interior numerical field, to be solved iteratively.

[1]The homogeneous conductivity profile, i.e., $m = 0$, is achieved by $\zeta \to \infty$ and $m \to \infty$.

[2]This is possible owing to the staggered grid.

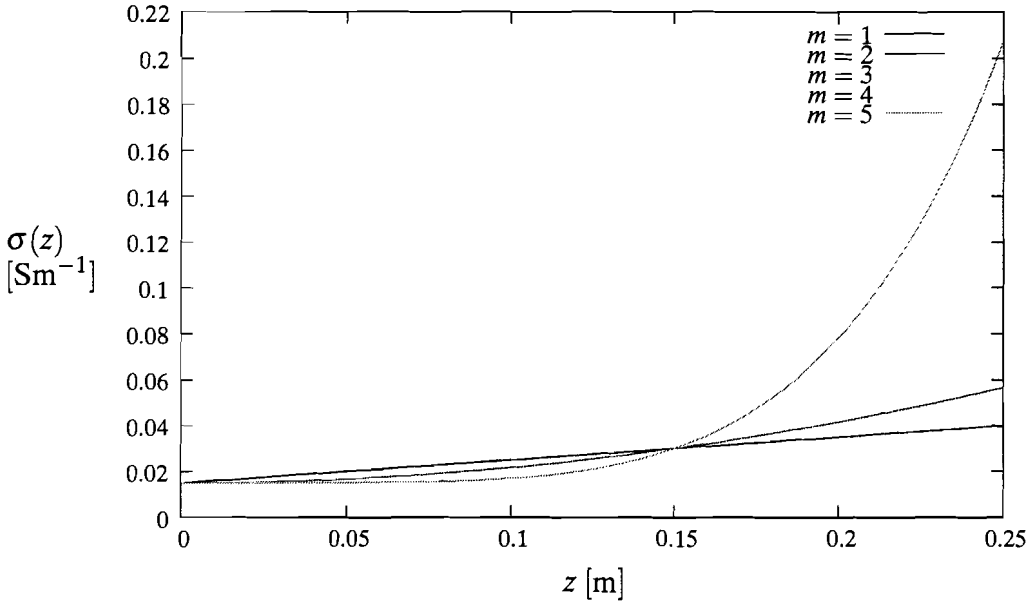

(a) Conductivity profiles in the PML

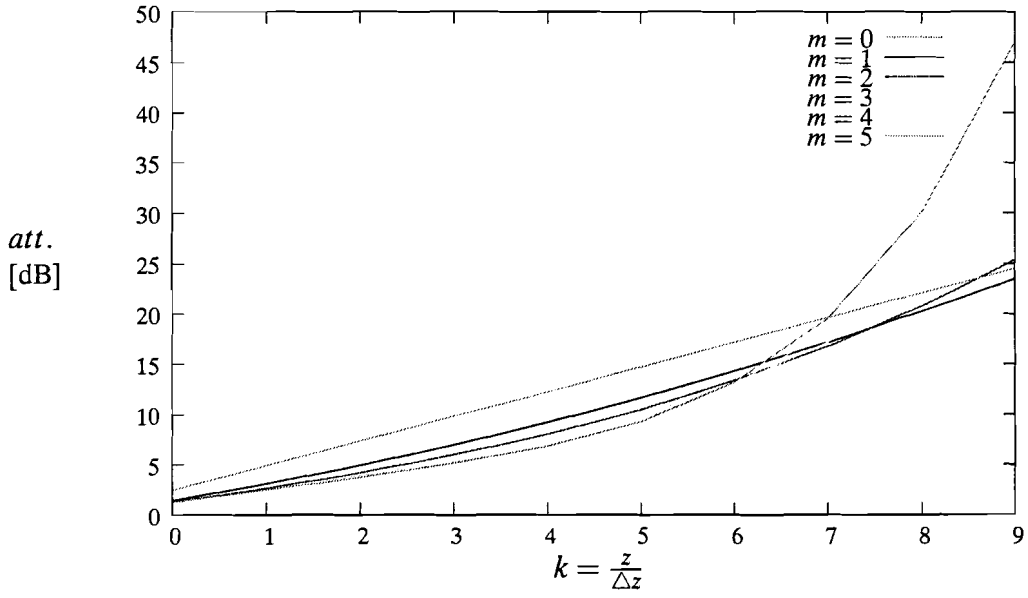

(b) Attenuation in the PML

Figure 4.2: Conductivity profiles and their corresponding attenuation in the PML for $\sigma_0^E = 1.5 \cdot 10^{-2}$ [Sm^{-1}], $m = 1 \ldots 5$, $\zeta = 0.15$. The distance z is normalised, i.e., $z = 0$ corresponds with the transition layer between background and PML.

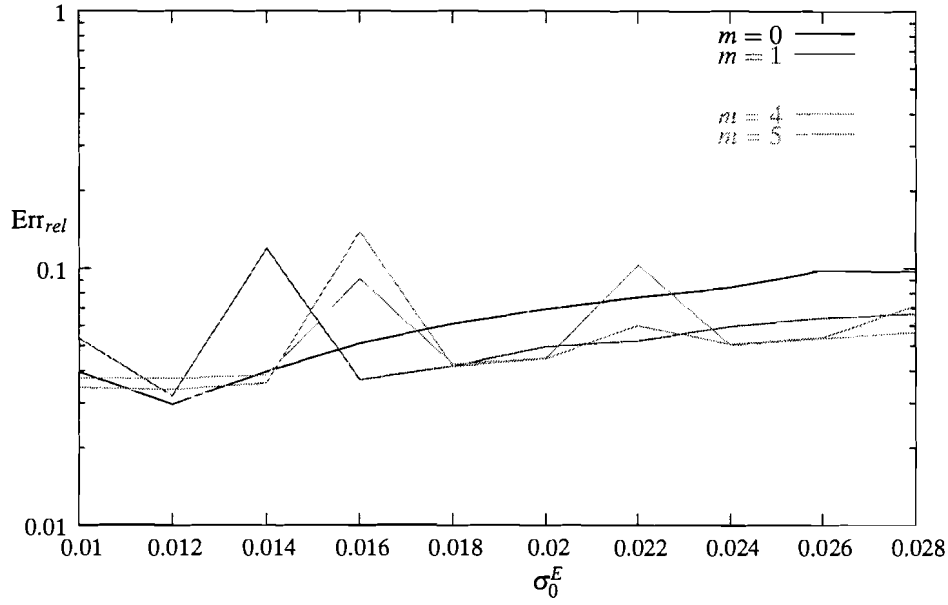

Figure 4.3: Relative errors of the numerical modal field compared to the analytical modal field, for various conductivity profiles with variable conductivity.

4.1.3 Results

Figure 4.3 shows the relative error of the numerical interior modal field compared to the analytical interior modal field, for five conductivity profiles of the PML, each with varying conductivity. Except for the homogeneous conductivity profile, these curves do not exhibit the expected monotonicity. This is probably due to the fact that the equivalent volume source (i.e., b') does not correspond with the actual boundary values of the numerical modal field in case of reflection from the PEC-boundary behind the equivalent volume source. This reflection will not be attenuated due to the presence of the absorbing boundary layer on the opposite open end *only*.

Figures 4.4 and 4.6 show the absolute values of the non-zero components of the numerical and analytical interior modal field, computed with $\sigma_0^E = 1.5 \cdot 10^{-2}[\mathrm{Sm}^{-1}]$ and $m = 2$. As expected from the relative error, shown in Figure 4.3, the modal field in the background region looks very similar to the analytical modal field. It can be seen that the tangential components of the modal field are continuous across the transition layer between the background and the PML, in correspondence with Equations (3.35a) and (3.35b). Since the discontinuity of $|H_z|$ equals approximately the discontinuity of μ_z across the transition layer, $|B_z|$ is expected to satisfy continuity condition (3.36a). Furthermore, the attenuation in the boundary layer is also clearly visible. For the tangential components, this attenuation seems to be exponential as expected. At a first glance, this does not seem to be the case for the attenuation of $|H_z|$. However, this cannot be concluded from the figure, since the attenuation of this field component might be exponental for each layer of the PML, while being discontinuous across the transition with the next layer. What ever be the case, this field component is attenuated sufficiently at the end of the PML. The con-

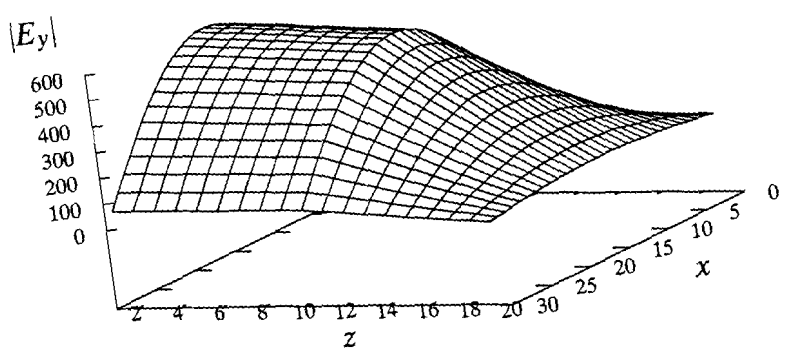

(a) numerical

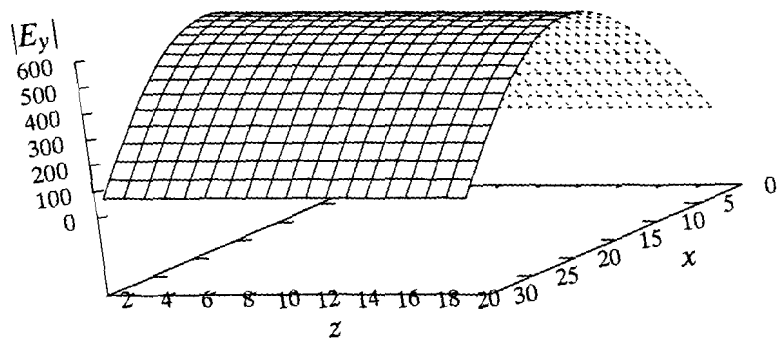

(b) analytical

Figure 4.4: The $|E_y|$ component of the modal field in the xz-plane at $y = 0$

4.1. MODAL FIELD

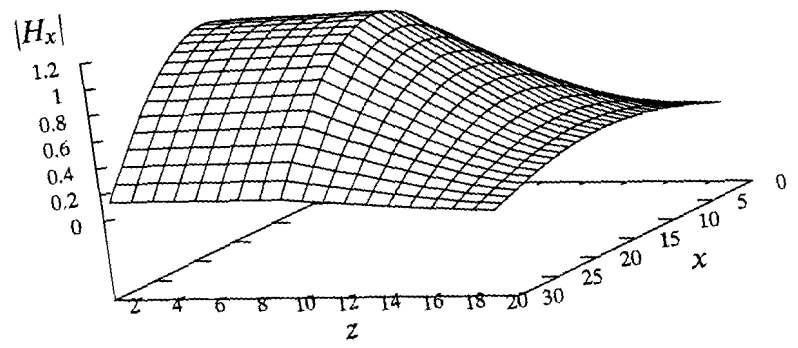

(a) numerical

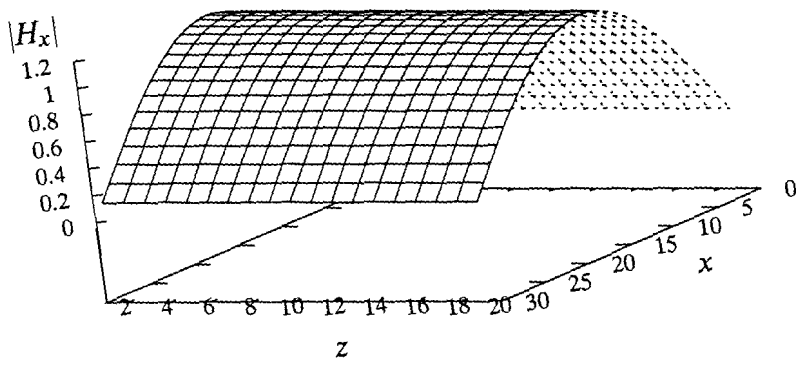

(b) analytical

Figure 4.5: The $|H_x|$ component of the modal field in the xz-plane at $y = 0$

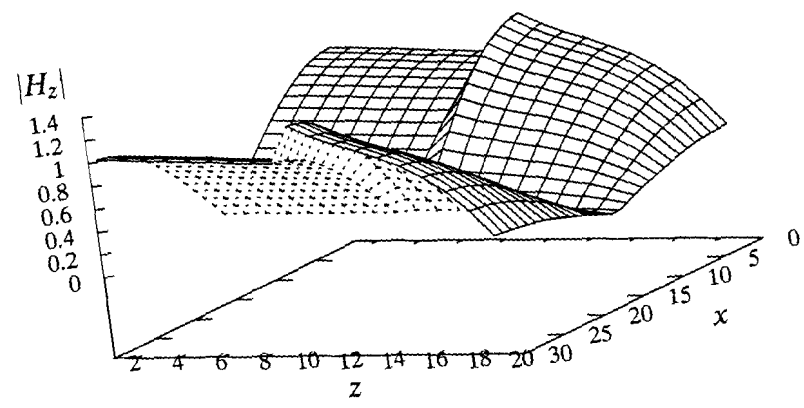

(a) numerical

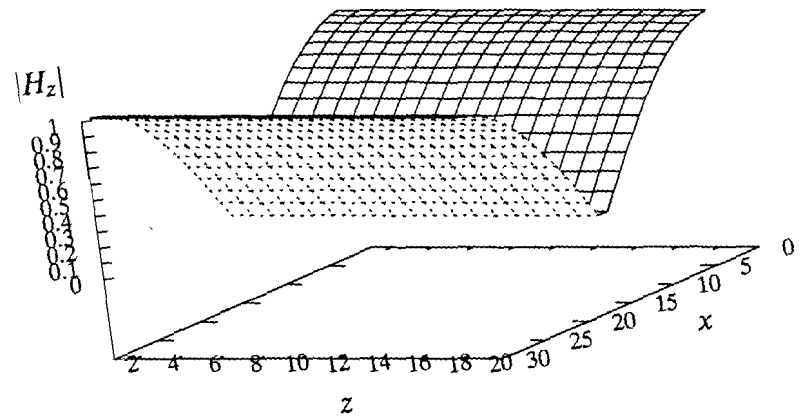

(b) analytical

Figure 4.6: The $|H_z|$ component of the modal field in the xz-plane at $y = 0$

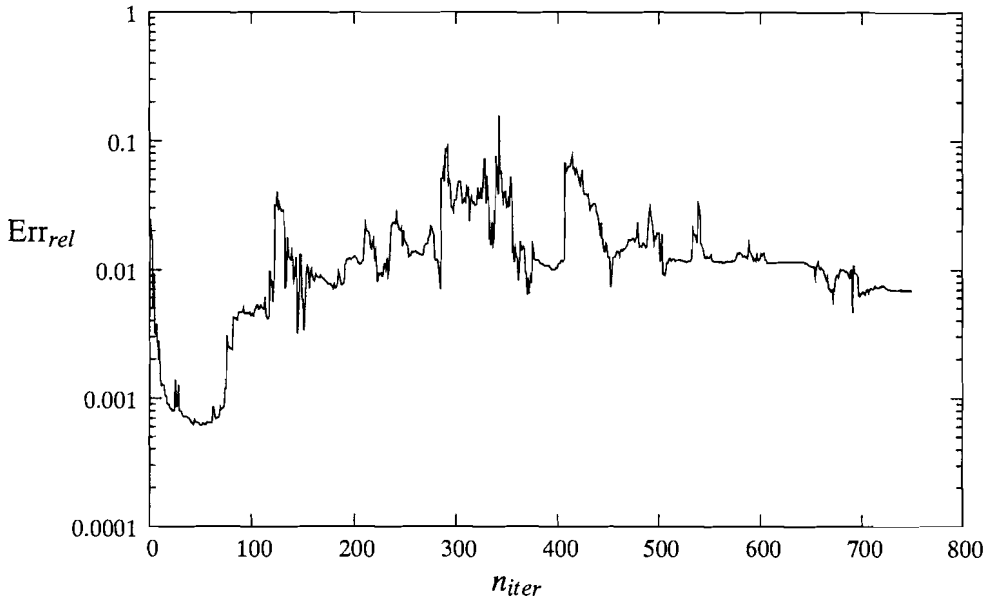

Figure 4.7: Convergence of the iterative solution to the modal field. Despite the quite erratic curve of convergence and despite increase of the relative error after the 50-th iteration, the iterative solution does converge to the modal field.

clusion can therefore be drawn that the finite-difference scheme, with the chosen conductivity profile of the PML, correctly and accurately computes the (numerical) interior modal field from its (analytic) boundary values.

The convergence of the iterative solution to the modal field is shown in Figure 4.7. This figure shows an approximately monotone decrease of the relative error until the 50-th iteration, after which the relative error increases and the convergence becomes quite erratic. This due to the fact that, until the 50-th iteration, the numerically propagating iterative solution has not reached the PEC boundary yet. Reflections from this boundary are therefore not taken into account, while the iterative solution already does satisfy the larger part of the finite-difference equations. However, this iterative solution does not correspond to the modal field and hence, the relative error of the iterative solution, as defined by Equation (4.1), does not represent the relative error of the numerical field compared to the analytical field. From the 50-th iteration on, the numerical reflections are taken into account. Therefore the iterative solution increases quite monotonously, until just after the 100-th iteration. From then on, the convergence becomes erratic. This is due to the reflections on the PEC-boundary behind the equivalent source, of the waves already reflected from the opposite boundary. These reflections now have the same direction of propagation as the expanded analytical modal field, and are therefore added to this field. This causes the relative error of the iterative solution not to decrease any further. Based on the above observations and the reasonably low relative errors of the numerical field compared to the analytical one, the conclusion can be drawn that the relative error of the iterative solution does measure the relative error of the numerical solution compared to the analytical one, as long as the number of iterations is chosen

several times the dimensions of the domain of computation in the direction of propagation.

4.2 Truncated Dipole field

This section presents the numerical validation of the reconstruction of a dipole field, being considered as a scattered field, from its decomposition to a regular and a singular field. For this, the dipole field will be truncated, thereby constructing the singular field. The regular field can now be constructed numerically from the secondary sources, created in the transition region of the truncation function. Since the scattered field is represented entirely by the singular field in the region where the truncation function equals unity, the regular field must vanish there[3]. This will be the main objective of this section.

4.2.1 Experiment

Maxwell's equations for the decomposed field state:

$$[\mathbf{M}]\begin{pmatrix}\mathbf{E}\\ \mathbf{H}\end{pmatrix}^{dip} = [\mathbf{M}]\begin{pmatrix}\mathbf{E}\\ \mathbf{H}\end{pmatrix}^{reg} + [\mathbf{M}]\begin{pmatrix}\mathbf{E}\\ \mathbf{H}\end{pmatrix}^{sng} = \begin{pmatrix}\mathbf{0}\\ \mathbf{J}^{dip}\end{pmatrix} \quad \text{on } \mathbb{R}^3. \tag{4.7}$$

In the transition region, the singular field will create secondary sources:

$$[\mathbf{M}]\begin{pmatrix}\mathbf{E}\\ \mathbf{H}\end{pmatrix}^{sng} = \begin{cases} [\mathbf{M}]\begin{pmatrix}\frac{1}{j\omega\tilde{\varepsilon}}\{\nabla\nabla\cdot+k^2\}\\ \nabla\times\end{pmatrix}\mathbf{A} = [\mathbf{M}]\begin{pmatrix}\mathbf{E}\\ \mathbf{H}\end{pmatrix}^{dip} & \text{on } \Omega_1, \\ [\mathbf{M}]\begin{pmatrix}\frac{\chi}{j\omega\tilde{\varepsilon}}\{\nabla\nabla\cdot+k^2\}\\ \chi\nabla\times\end{pmatrix}\mathbf{A} =: \begin{pmatrix}\mathbf{K}^s\\ \mathbf{J}^s\end{pmatrix} & \text{on } \Omega_\chi, \\ \begin{pmatrix}\mathbf{0}\\ \mathbf{0}\end{pmatrix} & \text{elsewhere,} \end{cases} \tag{4.8}$$

where Ω_1 is the region where $\chi = 1$ and Ω_χ is the transition region where $0 \leq \chi < 1$, i.e., where χ starts to truncate.

Since the Hertzian dipole produces electromagnetic fields satisfying the radiation conditions, the solution of Equation (4.7) will exist and will be unique, and hence the Maxwell operator is assumed to be invertable for exterior solutions. The regular field can therefore be constructed from the secondary sources:

[3]For "real" scattering problems, only the discontinuous field components will vanish in this region. The continuous field components will not vanish.

$$\begin{pmatrix}\mathbf{E}\\ \mathbf{H}\end{pmatrix}^{reg} = \begin{cases} [\mathbf{M}]^{-1}\begin{pmatrix}\mathbf{0}\\ \mathbf{J}^{dip}\end{pmatrix} - \begin{pmatrix}\mathbf{E}\\ \mathbf{H}\end{pmatrix}^{sng} = \begin{pmatrix}\mathbf{0}\\ \mathbf{0}\end{pmatrix} & \text{on } \Omega_1, \\ [\mathbf{M}]^{-1}\begin{pmatrix}\mathbf{0}\\ \mathbf{J}^{dip}\end{pmatrix} - [\mathbf{M}]^{-1}\begin{pmatrix}\mathbf{K}^s\\ \mathbf{J}^s\end{pmatrix} & \text{on } \Omega_\chi, \\ [\mathbf{M}]^{-1}\begin{pmatrix}\mathbf{0}\\ \mathbf{J}^{dip}\end{pmatrix} = \begin{pmatrix}\mathbf{E}\\ \mathbf{H}\end{pmatrix}^{dip} & \text{elsewhere.} \end{cases} \tag{4.9}$$

If now the secondary sources are taken into account for the entire domain $\mathbb{R}^3$, the equation to be solved for the regular field becomes:

$$[\mathbf{M}]\begin{pmatrix}\mathbf{E}\\ \mathbf{H}\end{pmatrix}^{reg} = -\begin{pmatrix}\mathbf{K}^s\\ \mathbf{J}^s\end{pmatrix} \tag{4.10}$$

As stated in the previous chapter, the transition region should not be chosen too small with respect to the mesh size. Also, the region where the truncation function equals unity should not be too small. By implementation of the truncation function, this region should at least contain six cells of the structured grid. However, from visual inspection of the secondary sources, the following restrictions have been found:

$$\Omega_\chi \geq 10\triangle h \tag{4.11}$$
$$\Omega_1 \geq 16\triangle h \tag{4.12}$$

for each direction x, y and z. The relatively large region where the truncation function equals unity is due to the singularity of the dipole field: the magnetic field is $O(\frac{1}{R^2})$ singular, the electric field is $O(\frac{1}{R^3})$ singular. The expectation is that this size can be chosen smaller when the scattered field is less singular, which is the case for scattering problems with a surface or a wire as scattering objects.

The following configuration has been chosen, with an equal PML as for the numerical computation of the modal field. The dipole placed in the center of the domain of computation:

- Dimensions of the domain: 2.5x2.5x2.5 [m].
- Grid size: 0.025x0.025x0.025 [m].
- $N_{PML} = 10$ (for each face).
- $\sigma_0 = 1.5 \cdot 10^{-2}$ [Sm^{-1}].
- $\zeta = 0.15$.
- $m = 2$.

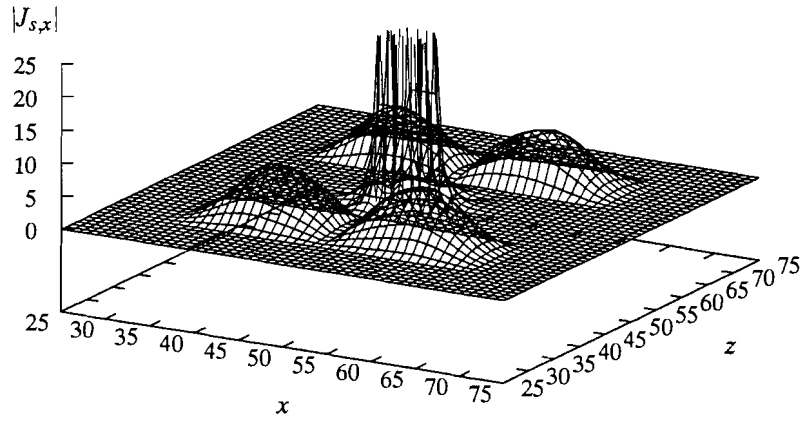

Figure 4.8: $J_{s,x}$ in the xz-plane at $y = y_{dip}$ with its singularity due to the singular dipole field. As can be seen, the minimum size of the region Ω_1 is limited by this singularity.

- $\mathbf{r}^{dip} = (1.0, 1.0, 1.0)$ [m].
- $\mathbf{u}_p = \mathbf{u}_z$.
- $f = 300$ [MHz].
- $\Omega_\chi = 0.25$x0.25x0.25 [m].
- $\Omega_1 = 0.4$ [m].

This yields a free space of 0.35 [m] between the truncation region and the PML. This might seem small, but since the secondary sources are smooth by construction, no field discontinuities are present in the vicinity of the PML.

4.2.2 Results

As stated before, the dipole field is heavily singular, requiring Ω_1 to be large. This singularity is depicted in Figure 4.8, together with the x-component of the electric secondary source in the xz-plane. This discontinuity defines the minimum size of Ω_1, i.e., the domain where the truncation function equals unity. The lower the order of the singularity of the scattered field, the better the numerical approximation of this field and hence the smaller the region where the Maxwell operator results in a zero-field will be. Therefore, the expectation is that the lower the order of singularity, the smaller the truncation region can be.

The method requires the dipole source to be cut-out from the domain of computation, since the regular field is computed numerically from the secondary sources only. Two components of these secondary sources in the xy-plane, at $z = z_{dip}$, are shown in Figure 4.9. It can be seen that these sources are smooth in $\mathbb{R}^3$, as required by the finite-difference method.

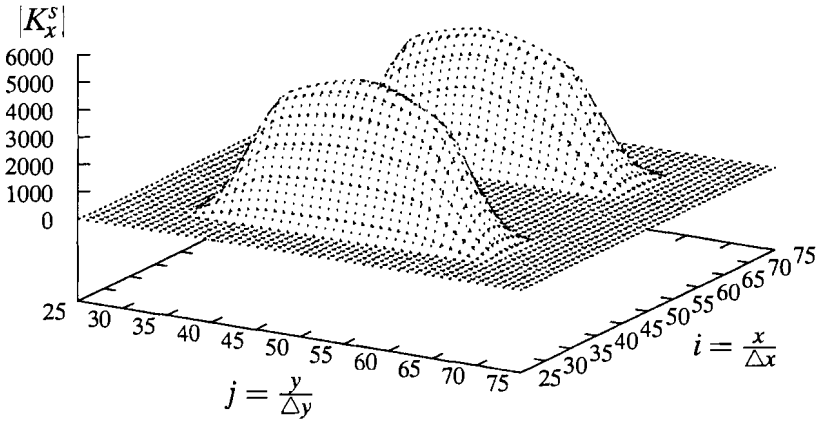

(a) $|K_{s,x}|$ in the xy-plane at $z = z_{dip}$

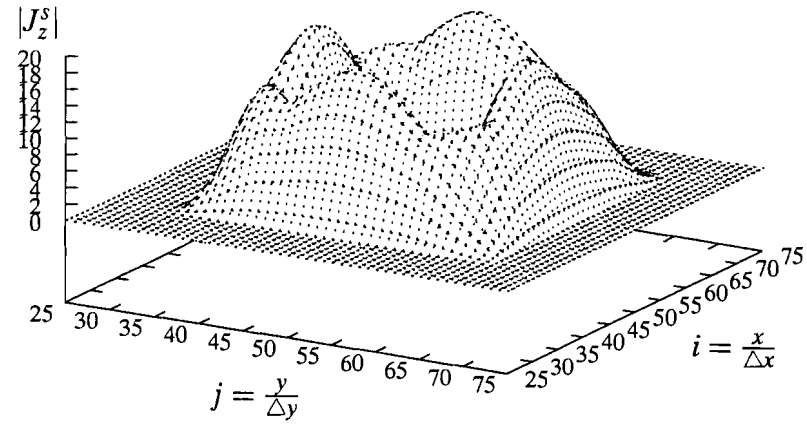

(b) $|J_{s,z}|$ in the xy-plane at $z = z_{dip}$

Figure 4.9: Two examples of the secondary sources for the regular field. With the chosen configuration, these sources are smooth.

Next, Equation (4.9) is solved numerically, which yields the regular field. The composition of this regular field and the singular field, together with the analytical dipole field, are depicted in Figure 4.10. The resulting regular field, together with the corresponding singular field, is depicted in Figure 4.11, where the singularity of the electric dipole field has not been visualised entirely. Only the region of interest is shown, i.e., the truncation region. Although the entire domain of computation is not shown in this figure, it shows that the regular field is smooth in the region where the secondary sources are present. It also shows that the regular field vanishes on Ω_1, i.e., the region where the truncation function equals unity.

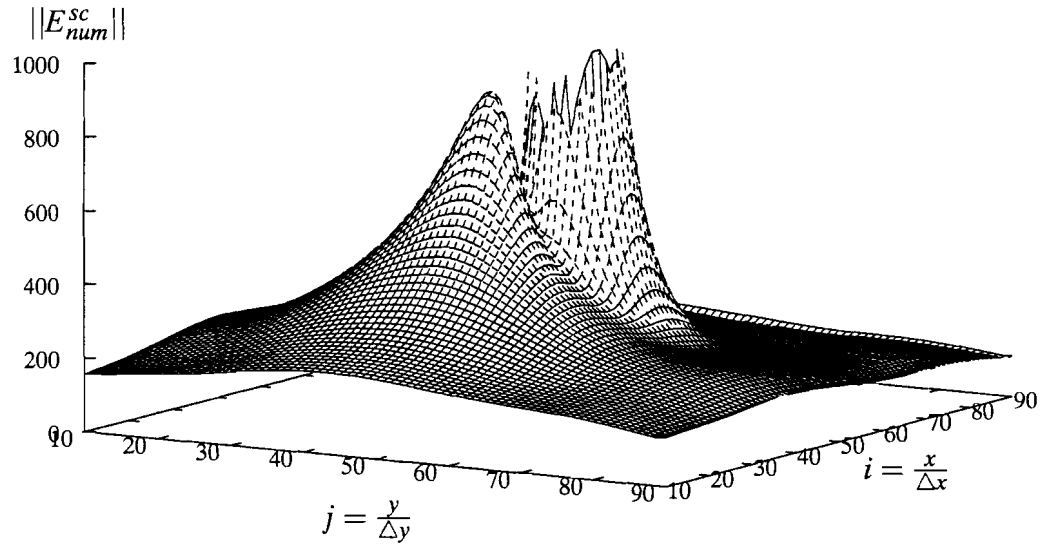

(a) numerical dipole field

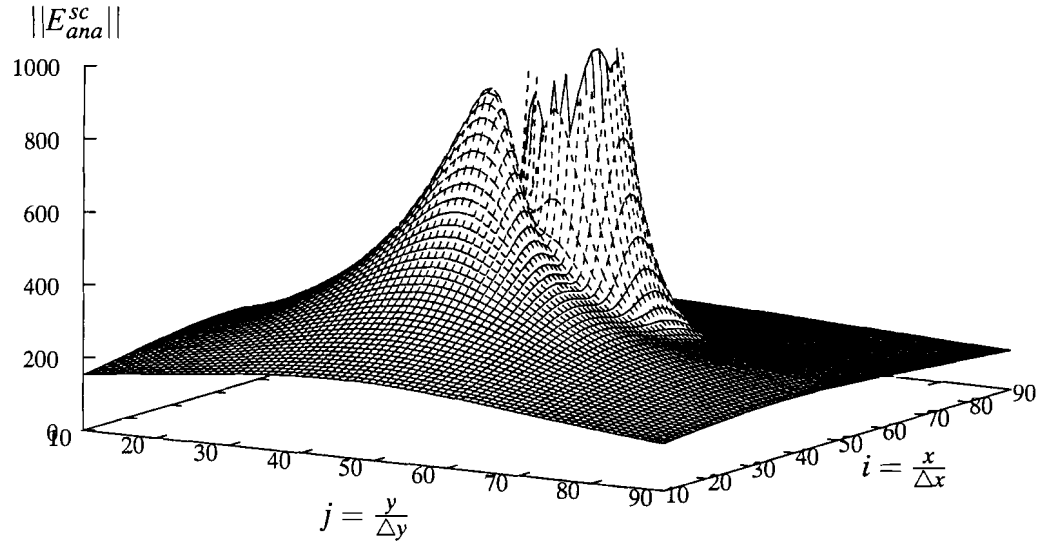

(b) analytical dipole field

Figure 4.10: The electric dipole field in the background. For clarity, the singularity of the dipole field is only partially visualised. The numerical dipole field has been obtained by the composition of the singular field and the regular field, where the latter has been computed from the secondary sources. The numerically field is a good approximation of the analytic field. Only at the interface between background and PML, a negligable discontinuity can be observed.

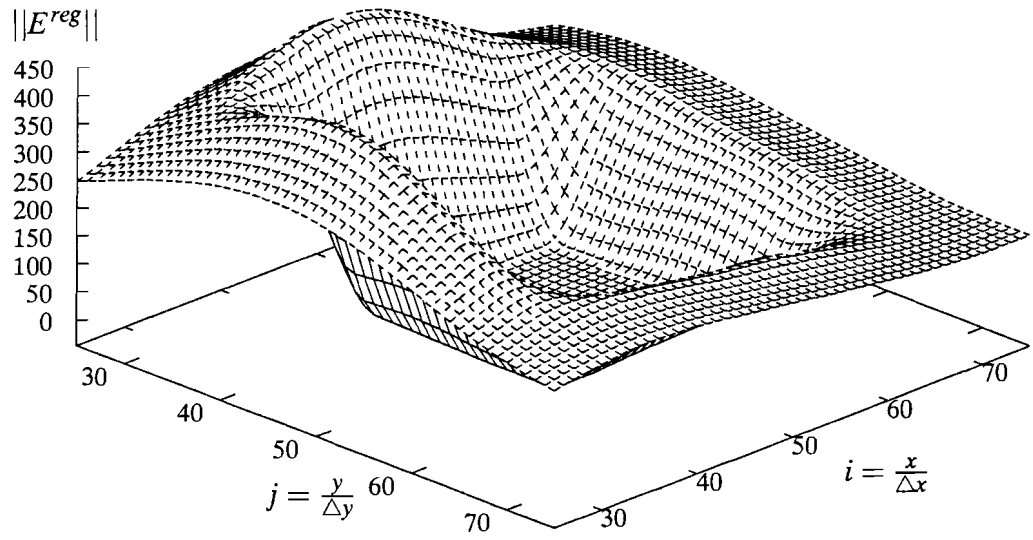

(a) $||\mathbf{E}^{reg}||$ in the xy-plane

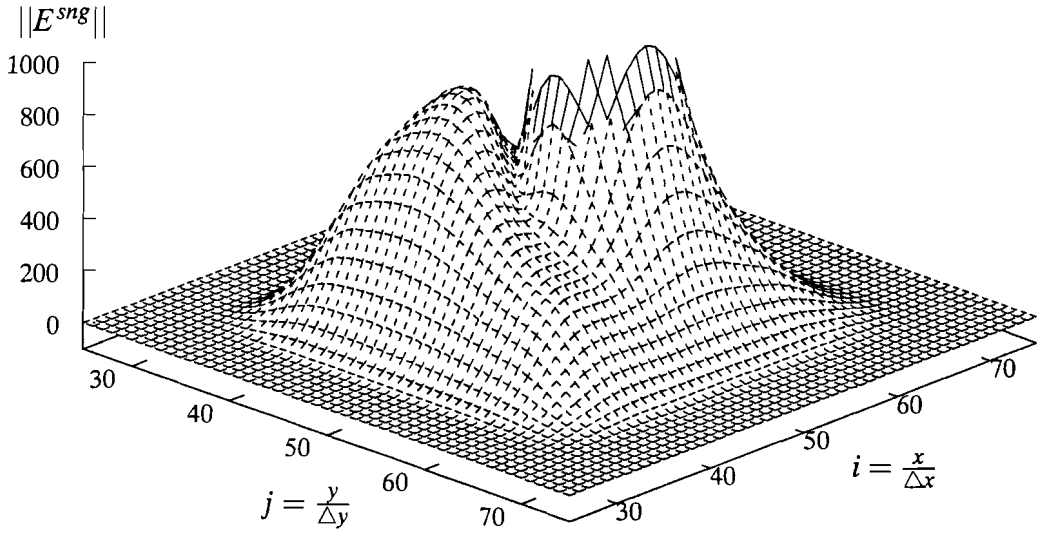

(b) $||\mathbf{E}^{sng}||$ in the xy-plane

Figure 4.11: The regular field and the singular field in the xy-plane, at $z = z_{dip}$. The truncation region is the only region of interest, therefore this region (and a little more) is shown only. It can be seen that the regular field vanishes in Ω_1, i.e. where the truncation function equals unity.

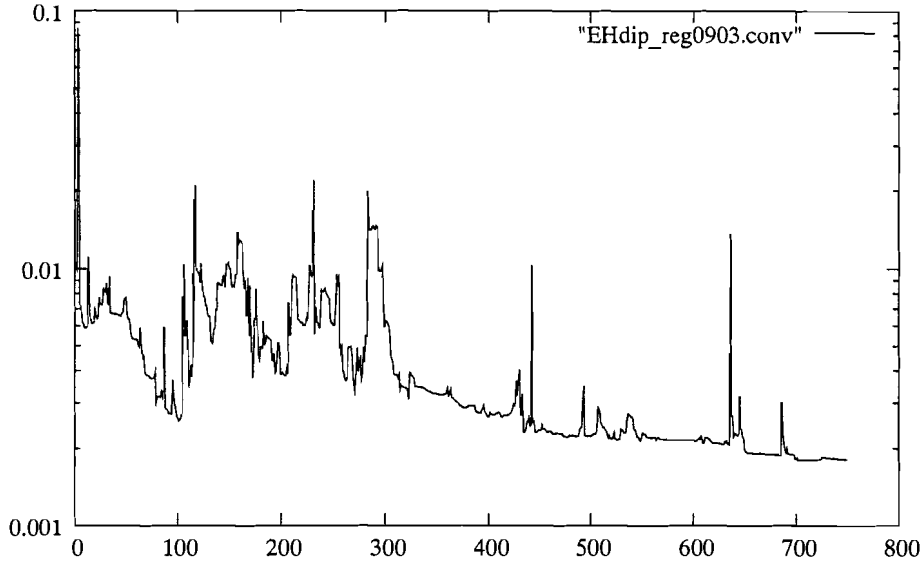

Figure 4.12: Convergence of the iterative solution to the regular field..

The converge of the iterative solution to the regular field is depicted in Figure 4.12. As with the converge of the iterative solution to the modal field (see Figure 4.7), this convergence is quite erratic. This is again due to the fact that, outside the truncation region, the secondary sources represent the *radiating* dipole field. In case of unsufficient attenuation of reflection from the PEC-boundary or in case of reflections due to the numerical mismatch of the PML itself, the secondary sources no longer represent the numerically computed radiating dipole field and hence Maxwell's equations are no longer satisfied. The same rule of thumb for the correspondence of the relative error of the iterative solution to the relative error of the numerical field compared to the analytical field can be applied: these two relative errors correspond if the number of iterations equals several times the mesh size in the direction of propagation.

Although not important for this study, a remarkable (at least to me) observation has been made concerning the numerical reconstruction of a dipole field. The dipole field in the interior domain can be computed numerically by the finite-difference method from its boundary values, i.e., the tangential components of the electric field on the boundary of the domain of computation, in the same way as the interior modal field has been computed. This implies that also the electric dipole itself can be reconstructed numerically, which seems to be in contradiction with the fact that the inverse boundary-value problem is not well posed (due to possible non-radiating sources). The correct numerical computation of the interior dipole field can be explained by the observation that non-radiating sources cannot be reconstructed numerically for the same reasons the hybrid method has been studied: the finite-difference method requires the electromagnetic field to be smooth.

Chapter 5

Conclusions and Recommendations

Modelling a thin PEC-scatterer as an infinitesimally thin wire or surface allows the formulation of a scattering problem as a boundary-value problem for the scattered electromagnetic field in $\mathbb{R}^3$. This scattered field can be decomposed in a singular field and a regular field, the former containing the discontinuity of the scattered field exactly and being localised in a small region around the scatterer, the latter being smooth in $\mathbb{R}^3$. The smooth truncation of the integral representation of the scattered field seems to be the best definition of the singular field, for reasons of smoothness of the coupling equations between the finite-difference method and the integral-equation method. The truncation of the scattered field and that of the surface-current density must be partitioned for the method to be useful. When these two truncation functions are chosen to be equal on the scatterer, their implementation is simplified. With this choice, the trace of the two truncation functions on the scatterer is not constant, causing extra terms to arise in the Galerkin discretisation of the integral equation. However, these terms can partially be calculated analytically, the other part is already calculated numerically in the other terms.

Rather than being a point of departure itself, the interpretation of the PML as a boundary layer of diagonally anisotropic, lossy material follows from a proper choice of the associated pull-back transformation of Maxwell's equations for the analytically continuated electromagnetic field. This choice of the transformation enables a relatively simple implementation of the numerical radiation conditions by nothing but a complex scaling of the material properties in the boundary layer. An augmenting loss in the PML, towards the boundary of the domain of computation, results in a better numerical approximation of the radiation conditions.

The optimal values of the various parameters of the PML have been obtained by simulating a modal field in an infinite waveguide. When one open end of this waveguide is simulated by applying the numerical radiation conditions to one face of the boundary of the domain of computation, and the other open end by expanding the boundary values of a propagating modal field on the opposite face, the convergence will become erratic due to (numerical) reflections. These reflections cause the expanded boundary values to no longer correspond with the interior electromagnetic field. However, when the number of iterations is chosen to equal at least twice the number of field samples in the direction of propagation, the resulting relative error of the iterative

method will be a good measure for the relative error of the numerically computed field.

The numerical reconstruction of a dipole field, which can be considered as a scattered field, from the composition of its regular field and its singular field, allows for a straightforward study of the truncation function and that of the field decomposition. The numerical experiments show that the secondary sources, for the regular field, are smooth and that the regular field vanishes where the scattered field is determined entirely by the singular field, i.e., where the truncation function equals unity. The strong singularity of the dipole field causes this region to be relatively large. However, since the electromagnetic field scattered from a surface or a wire is less singular than that of a dipole, this region can probably be chosen smaller with "real" scattering problems. Since the secondary sources for the regular field represent only the radiation of the dipole field, erratic convergence will occur in case of (numerical) reflections. Therefore, as with the computation of the modal field, the number of iterations should be twice the maximum number of field samples in one direction.

For the method to be applicable to "real" scattering problems, the combination of the partitioned truncation of the surface-current density and that of the singular field must be verified numerically. This might introduce more sophisticated truncation functions. An implementation in the time domain is also recommended for further study.

Appendix A

Vector Identities

A.1 Identities involving vector fields

Let $\mathbf{A}$ and $\mathbf{B}$ be smooth vector fields on R^3, let a be a scalar variable, and let $\mathbf{n}$ be the constant normal vector on the surface of an orientable object in R^3. Then the following identities are used (see [15,22]):

$$\nabla \times (a\mathbf{B}) = \nabla a \times \mathbf{B} + a\nabla \times \mathbf{B} \tag{A.1}$$
$$\nabla \cdot (a\mathbf{B}) = a\nabla \cdot \mathbf{B} + \mathbf{B} \cdot \nabla a \tag{A.2}$$
$$\nabla \cdot (a\mathbf{B}) = a\nabla \cdot \mathbf{B} + \mathbf{B} \cdot \nabla a \tag{A.3}$$
$$\nabla \times (\nabla a) = \mathbf{0} \tag{A.4}$$
$$\nabla \cdot (\nabla \times \mathbf{A}) = 0 \tag{A.5}$$
$$\nabla \times \nabla \times (\mathbf{A}) = \nabla\nabla \cdot \mathbf{A} - \triangle\mathbf{A} \tag{A.6}$$
$$\nabla_s \cdot (\mathbf{n} \times \mathbf{A}) = -\mathbf{n} \cdot (\nabla_s \times \mathbf{A}) \tag{A.7}$$
$$\mathbf{n} \times \nabla \times \mathbf{A} = \nabla_s(\mathbf{n} \cdot \mathbf{A}) - (\mathbf{n} \cdot \nabla)\mathbf{A}_s \tag{A.8}$$

A.2 Identities involving the plane wave

Let $\mathbf{E}_0$ be a constant vector field and let $k := \mathbf{k} \cdot \mathbf{k}$, then $\mathbf{E} = \mathbf{E}_0 e^{-j\mathbf{k}\cdot\mathbf{r}}$ is a plane wave. For this plane wave, the following identities hold:

$$\nabla \times \left(\mathbf{E}_0 e^{-j\mathbf{k}\cdot\mathbf{r}}\right) = -j\mathbf{k} \times \left(\mathbf{E}_0 e^{-j\mathbf{k}\cdot\mathbf{r}}\right), \tag{A.9}$$
$$\triangle\mathbf{E}_0 e^{-j\mathbf{k}\cdot\mathbf{r}} = -k^2\mathbf{E}_0 e^{-j\mathbf{k}\cdot\mathbf{r}}. \tag{A.10}$$

A.3 Identities involving the position vector

Let $\mathbf{r}$ be the position vector on R^3, let $R := ||\mathbf{r}||$ the distance as defined in Chapter 2 and let $G_{\mathbf{r}}$ be the frequency domain Green function on R^3. Then the following identities are used:

$$\nabla(R) = \frac{\mathbf{r}}{R} =: \mathbf{u}_r \tag{A.11}$$

$$\nabla(\frac{1}{R}) = -\frac{\mathbf{u}_r}{R^2} \tag{A.12}$$

$$\nabla G_{\mathbf{r}} = -(\frac{1}{R^2} + \frac{jk}{R})G_{\mathbf{r}}R\mathbf{u}_r =: -G_{\mathbf{r}}{}'R\mathbf{u}_r \tag{A.13}$$

$$\nabla G_{\mathbf{r}}{}' = \frac{\mathbf{u}_r}{R}(2G_{\mathbf{r}}{}' - k^2 G_{\mathbf{r}}) \tag{A.14}$$

$$\mathbf{r}_1 \times (\mathbf{r}_2 \times \mathbf{r}_3) = \mathbf{r}_2(\mathbf{r}_1 \cdot \mathbf{r}_3) - \mathbf{r}_3(\mathbf{r}_1 \cdot \mathbf{r}_2) \tag{A.15}$$

Appendix B

Oblique-incidence reflection problem

A reflection problem for a plane wave with oblique incidence on the interface between the homogeneous, isotropic, lossless background medium and the homogeneous, axially anisotropic lossy PML is elaborated in this chapter. The incident field will be a plane wave:

$$\mathbf{E} = \mathbf{E}_0 e^{-j\mathbf{k}\cdot\mathbf{r}}, \tag{B.1a}$$

$$\mathbf{H} = \mathbf{H}_0 e^{-j\mathbf{k}\cdot\mathbf{r}}. \tag{B.1b}$$

The analytic continuation of this field is:

$$\hat{\mathbf{E}} = \hat{\mathbf{E}}_0 e^{-j\mathbf{k}[V]\mathbf{r}}, \tag{B.2a}$$

$$\hat{\mathbf{H}} = \hat{\mathbf{H}}_0 e^{-j\mathbf{k}[V]\mathbf{r}}. \tag{B.2b}$$

From equations (3.42a) and (3.42b), the algebraic Maxwell equations can now be derived for the field in the PML:

$$[\Lambda]^{-1}[V]\mathbf{k}\times\hat{\mathbf{E}} - \omega\mu\hat{\mathbf{H}} = \mathbf{0}, \tag{B.3a}$$

$$[\Lambda]^{-1}[V]\mathbf{k}\times\hat{\mathbf{H}} + \omega\varepsilon\hat{\mathbf{E}} = \mathbf{0}, \tag{B.3b}$$

from which the dispersion relation can be obtained:

$$[G]^2(\mathbf{k}\cdot\mathbf{k}) = \omega^2\mu\varepsilon = k^2, \tag{B.4}$$

where $[G] := [\Lambda]^{-1}[V]$. Elaborating for the Cartesian components gives:

$$k^2 = (k_x\lambda_y\lambda_z)^2 + (k_y\lambda_z\lambda_x)^2 + (k_z\lambda_x\lambda_y)^2, \tag{B.5}$$

which can be solved according to [17] for the individual components:

$$k_x = \frac{k}{\lambda_y\lambda_z}\sin\theta\cos\phi, \tag{B.6a}$$

$$k_y = \frac{k}{\lambda_z\lambda_x}\sin\theta\sin\phi, \tag{B.6b}$$

$$k_z = \frac{k}{\lambda_x\lambda_y}\cos\theta. \tag{B.6c}$$

If now the propagation vectors are restricted to the xz-plane, which correspond to $\phi = 0$ and $k_y = 0$, the electromagnetic field can be decomposed into a TE-polarisation and a TM-polarisation. Only the TE-polarisation will be elaborated, [20] will be used to state the results for the TM-polarisation. The TE-polarised incident (^{i}), reflected (^{r}) and the transmitted (^{t}) electric field can now be written as:

$$\mathbf{E}^i = A_y^i \mathbf{u}_y e^{-j(k_x^i x + k_z^i z)}, \tag{B.7a}$$

$$\mathbf{E}^r = A_y^r \mathbf{u}_y e^{-j(k_x^r x + k_z^r z)}, \tag{B.7b}$$

$$\mathbf{E}'^t = A_y^t \mathbf{u}_y e^{-j(k_x' x + k_z' z)}, \tag{B.7c}$$

where the prime $'$ denotes the field in the PML. The corresponding magnetic waves can be found from equation (B.3a).

Elaborating jump condition (2.11b) for the electric field, while assuming the interface between the background medium and the PML at $z = 0$, results in:

$$A_y^i e^{-jk_x^i x} + A_y^r e^{-jk_x^r x} = A_y^t e^{-jk_x' x}. \tag{B.8}$$

Since an infinite interface is assumed, this equation must hold for *all* x, and therefore

$$k_x^i = k_x^r = k_x'. \tag{B.9}$$

Together with equation (B.6a), Snell's laws can be obtained:

$$\sin\theta_i = \sin\theta_r, \tag{B.10a}$$

$$\sin\theta_i = \frac{1}{\lambda_z \lambda_y} \sin\theta_t. \tag{B.10b}$$

Elaborating jump condition (2.11a) for the electric field, while still assuming the interface between the background medium and the PML at $z = 0$, results in:

$$\frac{(\mathbf{k}^i \times \mathbf{E}^i)_x}{\omega\mu} + \frac{(\mathbf{k}^r \times \mathbf{E}^r)_x}{\omega\mu} = [G]\frac{(\mathbf{k}^t \times \mathbf{E}^t)_x}{\omega\mu}, \tag{B.11}$$

which, together with equation (B.6a), can be elaborated to:

$$A_x^i \cos\theta_i - A_x^r \cos\theta_r = \frac{\lambda_y}{\lambda_x} A_x \cos\theta_t. \tag{B.12}$$

Solving the system of equations (B.8),(B.12) results in the reflection coefficient:

$$R^{TE} = \frac{\cos\theta_i - \frac{\lambda_y}{\lambda_x}\cos\theta_t}{\cos\theta_i + \frac{\lambda_y}{\lambda_x}\cos\theta_t}. \tag{B.13}$$

The reflection coefficient for the TM-polarisation is given by:

$$R^{TM} = \frac{\frac{\lambda_y}{\lambda_x}\cos\theta_i - \cos\theta_t}{\cos\theta_t + \frac{\lambda_y}{\lambda_x}\cos\theta_i}. \tag{B.14}$$

Now the PML can be made iso-reflective (i.e., a zero reflection of the incident field) by letting $\lambda_y^z = \frac{1}{\lambda_z^z}$ and $\lambda_x^z = \lambda_y^z$, as already stated by Equation (3.46).

Appendix C

Analytic fields

C.1 Dipole Field

The vector potential **A** is for the Hertzian dipole:

$$\mathbf{A} = A_{dip} G_{\mathbf{r}} \mathbf{u}_p \tag{C.1}$$

where $\mathbf{u}_p$ is the polarisation vector. Here, the z-polarisation will be used, so $\mathbf{u}_p = \mathbf{u}_z$. Substituting this potential in equation (2.29b), results in:

$$\mathbf{E}_{dip} = \frac{A_{dip}}{j\omega\bar{\varepsilon}} \{\nabla\nabla\cdot + k^2\} (G_{\mathbf{r}} \mathbf{u}_p) \tag{C.2}$$

Elaborating the derivatives, with the aid of the identities in Appendix A, yields:

$$\nabla\nabla\cdot (G_{\mathbf{r}} \mathbf{u}_p) = (\mathbf{u}_p \cdot \mathbf{u}_r)\mathbf{u}_r (2G_{\mathbf{r}}' - k^2 G_{\mathbf{r}}) \tag{C.3}$$

Since the factor $(\mathbf{u}_p \cdot \mathbf{u}_r)\mathbf{u}_r$ represents the longitudinal component, the aim is to decompose the term $k^2\mathbf{A}$ in a longitudinal and transversal component as well. With the observation that $(\mathbf{u}_r \cdot \mathbf{u}_r) = 1$, this leads to:

$$k^2 G_{\mathbf{r}} \mathbf{u}_p = k^2 G_{\mathbf{r}} \mathbf{u}_p (\mathbf{u}_r \cdot \mathbf{u}_r) = k^2 G_{\mathbf{r}} \left((\mathbf{u}_p \cdot \mathbf{u}_r)\mathbf{u}_r - \mathbf{u}_r \times \mathbf{u}_r \times \mathbf{u}_p\right) \tag{C.4}$$

Now the electric dipole field can be written as:

$$\mathbf{E}_{dip} = \frac{A_{dip}}{j\omega\bar{\varepsilon}} \left((\mathbf{u}_p \cdot \mathbf{u}_r)\mathbf{u}_r 2G_{\mathbf{r}}' - (\mathbf{u}_r \times \mathbf{u}_r \times \mathbf{u}_p) k^2 G_{\mathbf{r}}\right) \tag{C.5}$$

For the magnetic dipole field, the potential is substituted in Equation (2.29a). This results in:

$$\mathbf{H}_{dip} = \nabla \times \left(A_{dip} G_{\mathbf{r}} \mathbf{u}_p\right) = A_{dip} \nabla G_{\mathbf{r}} \times \mathbf{u}_p \tag{C.6}$$

Using the relation (A.13) and the chain rule of differentiation results in:

$$\mathbf{H}_{dip} = A_{dip} G_{\mathbf{r}}' \mathbf{r} \times \mathbf{u}_p, \tag{C.7}$$

C.2 Modal Field

Two polarisations can be present in a waveguide: TE and TM. For TE polarisation, the *mn*-th mode, propagating in the z-direction, is given by [20]:

$$E_x = \frac{Cj\omega\bar{\mu}}{\left(\frac{m\pi}{a}\right)^2+\left(\frac{n\pi}{b}\right)^2}\frac{n\pi}{b}\cos\left(\frac{m\pi}{a}x\right)\sin\left(\frac{n\pi}{b}y\right)e^{-\gamma_{mn}z} \tag{C.8a}$$

$$E_y = \frac{-Cj\omega\bar{\mu}}{\left(\frac{m\pi}{a}\right)^2+\left(\frac{n\pi}{b}\right)^2}\frac{m\pi}{a}\sin\left(\frac{m\pi}{a}x\right)\cos\left(\frac{n\pi}{b}y\right)e^{-\gamma_{mn}z} \tag{C.8b}$$

$$E_z = 0 \tag{C.8c}$$

$$H_x = \frac{C\gamma_{mn}}{\left(\frac{m\pi}{a}\right)^2+\left(\frac{n\pi}{b}\right)^2}\frac{m\pi}{a}\sin\left(\frac{m\pi}{a}x\right)\cos\left(\frac{n\pi}{b}y\right)e^{-\gamma_{mn}z} \tag{C.8d}$$

$$H_y = \frac{C\gamma_{mn}}{\left(\frac{m\pi}{a}\right)^2+\left(\frac{n\pi}{b}\right)^2}\frac{n\pi}{b}\cos\left(\frac{m\pi}{a}x\right)\sin\left(\frac{n\pi}{b}y\right)e^{-\gamma_{mn}z} \tag{C.8e}$$

$$H_z = C\cos\left(\frac{m\pi}{a}x\right)\cos\left(\frac{n\pi}{b}y\right)e^{-\gamma_{mn}z} \tag{C.8f}$$

and for TM polarisation:

$$E_x = \frac{-C\gamma_{mn}}{\left(\frac{m\pi}{a}\right)^2+\left(\frac{n\pi}{b}\right)^2}\frac{m\pi}{a}\cos\left(\frac{m\pi}{a}x\right)\sin\left(\frac{n\pi}{b}y\right)e^{-\gamma_{mn}z} \tag{C.9a}$$

$$E_y = \frac{-C\gamma_{mn}}{\left(\frac{m\pi}{a}\right)^2+\left(\frac{n\pi}{b}\right)^2}\frac{n\pi}{b}\sin\left(\frac{m\pi}{a}x\right)\cos\left(\frac{n\pi}{b}y\right)e^{-\gamma_{mn}z} \tag{C.9b}$$

$$E_z = C\sin\left(\frac{m\pi}{a}x\right)\sin\left(\frac{n\pi}{b}y\right)e^{-\gamma_{mn}z} \tag{C.9c}$$

$$H_x = \frac{Cj\omega\bar{\varepsilon}}{\left(\frac{m\pi}{a}\right)^2+\left(\frac{n\pi}{b}\right)^2}\frac{n\pi}{b}\sin\left(\frac{m\pi}{a}x\right)\cos\left(\frac{n\pi}{b}y\right)e^{-\gamma_{mn}z} \tag{C.9d}$$

$$H_y = \frac{-Cj\omega\bar{\varepsilon}}{\left(\frac{m\pi}{a}\right)^2+\left(\frac{n\pi}{b}\right)^2}\frac{m\pi}{a}\cos\left(\frac{m\pi}{a}x\right)\sin\left(\frac{n\pi}{b}y\right)e^{-\gamma_{mn}z} \tag{C.9e}$$

$$H_z = 0 \tag{C.9f}$$

In both polarisations, the propagation constant γ_{mn} is given by [20]:

$$\gamma_{mn} = \sqrt{\left(\frac{n\pi}{b}\right)^2+\left(\frac{m\pi}{a}\right)^2-\left(\frac{\omega}{c}\right)^2} \tag{C.10}$$

Frequencies resulting in propagative modes are below cut-off; above this frequency modes are attenuative. Expressing the cut-off frequency in m, n and waveguide dimensions result in a circle equation, see figure C.1.

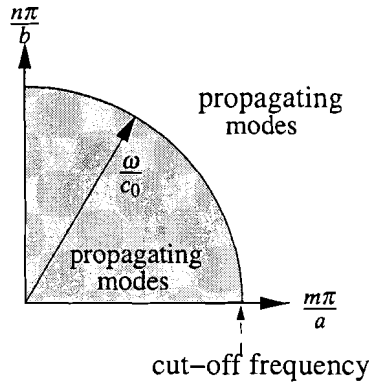

Figure C.1: Region of frequencies below cut-off, parametrised by the dimensions of the wave guide.

Bibliography

[1] Genesis 1:3. http://en.wikipedia.org/wiki/Genesis_1:3.

[2] Robert A. Adams. *Sobolev Spaces.* Academic Press, 1975.

[3] J. P. Berenger. Perfectly matched layer for the solution of wave-structure interaction problems. *IEEE Transactions on Antennas and Propagation*, 44(1):110–117, January 1996.

[4] Vaughn Betz and Raj Mittra. A boundary condition to absorb both propagating and evanescent waves in a finite-difference time-domain simulation. *IEEE Microwave and Guided Wave Letters*, 3(6):182–184, June 1993.

[5] A.R. Bretones, R. Mittra, and R.G. Martin. A hybrid technique combining the method of moments in the time domain and FDTD. *IEEE Microwave and Guided Wave Letters*, 8(8):281–283, August 1998.

[6] A.R. Bretones, A. Monorchio, G. Manara, R. Gomez Martin, and R. Mittra. A hybrid time-domain technique that combines the finite element, finite difference and method of moment techniques to solve complex electromagnetic problems. *IEEE Transactions on Antennas and Propagation*, 52(10):2666–2674, Octobre 2004.

[7] W.C. Chew and W.H. Weedon. A 3-d perfectly matched medium from modified Maxwell's equations with stretched coordinates. *Microwave Optical Technicology Letters*, 7:599–604, September 1994.

[8] Thierry Dauxois and Michel Peyrard. La dernière expérience d'Enrico Fermi. *La Recherche*, 386:51–53, Mai 2005.

[9] Stephen D. Gedney. An anisotropic perfectly matched layer-absorbing medium for the truncation of FDTD lattices. *IEEE Transactions on Antennas and Propagation*, 44(12):1630–1639, December 1996.

[10] D.S. Jones. *Methods in Electromagnetic Wave Propagation.* Oxford : Clarendon Press, 2 edition, 1994.

[11] R.M.M. Mattheij, S.W. Rienstra, and J.H.M Ten Thije Boonkkamp. *Partial Differential Equations: Modeling, Analysis, Computation.* Society for Industrial & Applied Mathematics, 2005.

[12] Claus Müller. *Foundations of the Mathematical Theory of Electromagnetic Waves*, volume 155 of *Die Grundlehren der mathematischen Wissenschaften in Einzeldarstellungen*. Springer-Verlag, 1969.

[13] Gerrit Mur and Adrianus T. de Hoop. A finite-element method for computing three-dimensional electromagnetic field in inhomogeneous media. *IEEE Transactions on Magnetics*, MAG-21(6):2188–2191, November 1985.

[14] Sadasiva M. Rao, Donald R. Wilton, and Allen W. Glisson. Electromagnetic scattering by conducting surfaces of arbitrary shape. *IEEE Transactions on Antennas and Propagation*, 30(3):409–418, March 1982.

[15] Edward J. Rothwell and Michael J. Cloud. *Electromagnetics*. CRC Press, 2001.

[16] Yousef Saad. *Iterative Methods for Sparse Linear Systems*. PWS Publishing Company, 1996.

[17] Zachary S. Sacks, David M. Kingsland, Robert Lee, and Jin-Fa Lee. A perfectly matched anisotropic absorber for use as an absorbing boundary condition. *IEEE Transactions on Antennas and Propagation*, 43(12):1460–1463, December 1995.

[18] Lionel Ségui. *Sur un problème inverse en diffraction d'ondes*. PhD thesis, L'École Nationale Supérieure de l'Aéronautique et de l'Espace, Novembre 2000.

[19] Anton G. Tijhuis. Elektromagnetisme 2. Collegedictaat, November 1999. Vakcode: 5F080.

[20] Anton G. Tijhuis and Martijn C. van Beurden. Elektromagnetische golven en straling. Collegedictaat, February 2004. Vakcode: 5F100.

[21] Anton G. Tijhuis and A. Zwamborn. Computational electromagnetics. Collegedictaat. Vakcode: 5MH00.

[22] Martijn van Beurden. *Integro-differential equations for electromagnetic scattering*. PhD thesis, Eindhoven University of Technology, September 2003.

[23] Kane S. Yee. Numerical solution of inital boundary value problems involving maxwell's equations in isotropic media. *IEEE Transactions on Antennas and Propagation*, 14(3):302–307, May 1966.

[24] Li Zhao and Andreas C. Cangellaris. A general approach for the development of unsplit-field time-domain implementations of perfectly matched layers for FDTD grid truncation. *IEEE Microwave and Guided Wave Letters*, 6(5):209–211, May 1996.

[25] Li Zhao and Andreas C. Cangellaris. GT-PML: Generalized theory of perfectly matched layers and its application to the reflectionless truncation of finite-difference time-domain grids. *IEEE Transactions on Microwave Theory and Techniques*, 44(12):2555–2563, December 1996.

Samenvatting

De eindige differentie methode biedt een snelle, accurate en efficiënte methode voor het numeriek oplossen van randwaarde-problemen dankzij het gestructureerde, gestapelde rooster. Ondanks de noodzaak van numerieke uitstralingsvoorwaarden is de methode erg populair voor het berekenen van elektromagnetische verstrooiing. Desalniettemin weerspiegelt deze populariteit niet de toepasbaarheid van de methode voor een breed scala van problemen: wanneer het verstrooiende object willekeurig van vorm is, is het gestructureerd rooster niet langer conform en verliest de methode dientengevolge zijn precisie. In deze gevallen wordt vaak een integraalvergelijkings methode, gebaseerd op Galerkin discretisatie, gebruikt. Echter, de nadelen van deze methode zijn een numeriek dure matrix-inversie en een hoger gebruik van geheugen. Een hybride methode is bestudeerd geweest om te profiteren van de voordelen van beide methoden: conformiteit van het rooster aan de willekeurig gevormde verstrooier door de integraalvergelijkings methode, en precisie en efficiëntie door de eindige differentie methode. Zij is gebaseerd op een mathematische decompositie van het verstrooide veld door een gladde, gepartitioneerde truncatie-functie. De verwachting is dat deze partitionering een efficiënter matrix-vector product en dus een snellere convergentie oplevert ten opzichte van de reeds bestaande hybride methoden. De veld-decompositie en principiële werking van de hybride methode is numeriek geverifieerd geweest met een dipool-veld.